2009

Enhanced Dense Gas Fraction in Ultra-Luminous Infrared Galaxies

S. Juneau

Desika Narayanan
Haverford College, dnarayan@haverford.edu

Repository Citation

"Enhanced Dense Gas Fraction in Ultra-Luminous Infrared Galaxies" Juneau, S., Narayanan, D., Moustakas, J., Shirley, Y., Bussmann, R., Kennicutt, R., Vanden Bout, P., 2009, ApJ 707, 1217

The Astrophysical Journal, 707:1217–1232, 2009 December 20 doi:10.1088/0004-637X/707/2/1217

ENHANCED DENSE GAS FRACTION IN ULTRALUMINOUS INFRARED GALAXIES

S. Juneau[1], D. T. Narayanan[2,7], J. Moustakas[3,4], Y. L. Shirley[1], R. S. Bussmann[1], R. C. Kennicutt Jr.[5], and P. A. Vanden Bout[6]
[1] Steward Observatory, Department of Astronomy, University of Arizona, 933 N. Cherry Ave., Tucson, AZ 85721, USA; sjuneau@as.arizona.edu, yshirley@as.arizona.edu, rsbussmann@as.arizona.edu
[2] Harvard-Smithsonian Center for Astrophysics, 60 Garden St. MS 51, Cambridge, MA, 02138, USA; dnarayanan@cfa.harvard.edu
[3] Department of Physics, New York University, 4 Washington Place, New York, NY 10003, USA
[4] Center for Astrophysics and Space Sciences, University of California, San Diego, 9500 Gilman Drive, La Jolla, CA 92093-0424, USA; jmoustakas@ucsd.edu
[5] Institute of Astronomy, University of Cambridge, Madingley Road, Cambridge CB3 0HA, UK; robk@ast.cam.ac.uk
[6] National Radio Astronomy Observatory, 520 Edgemont Road, Charlottesville, VA 22903, USA; pvandenb@nrao.edu
Received 2009 August 25; accepted 2009 October 30; published 2009 December 3

ABSTRACT

We present a detailed analysis of the relation between infrared luminosity and molecular line luminosity, for a variety of molecular transitions, using a sample of 34 nearby galaxies spanning a broad range of infrared luminosities ($10^{10}\ L_\odot < L_{\rm IR} < 10^{12.5}\ L_\odot$). We show that the power-law index of the relation is sensitive to the critical density of the molecular gas tracer used, and that the dominant driver in observed molecular line ratios in galaxies is the gas density. As most nearby ultraluminous infrared galaxies (ULIRGs) exhibit strong signatures of active galactic nuclei (AGNs) in their center, we revisit previous claims questioning the reliability of HCN as a probe of the dense gas responsible for star formation in the presence of AGNs. We find that the enhanced HCN(1–0)/CO(1–0) luminosity ratio observed in ULIRGs can be successfully reproduced using numerical models with fixed chemical abundances and without AGN-induced chemistry effects. We extend this analysis to a total of 10 molecular line ratios by combining the following transitions: CO(1–0), $\rm HCO^+$(1–0), $\rm HCO^+$(3–2), HCN(1–0), and HCN(3–2). Our results suggest that AGNs reside in systems with higher dense gas fraction, and that chemistry or other effects associated with their hard radiation field may not dominate (NGC 1068 is one exception). Galaxy merger could be the underlying cause of increased dense gas fraction, and the evolutionary stage of such mergers may be another determinant of the HCN/CO luminosity ratio.

Key words: galaxies: evolution – galaxies: fundamental parameters – galaxies: ISM – infrared: galaxies – radio lines: galaxies – submillimeter

Online-only material: color figures, extended figure

1. INTRODUCTION

Over the past 50 years, there have been a number of studies relating galaxy star formation rate (SFR) and the amount of molecular gas available. Schmidt (1959) proposed a power-law relationship between star formation rate volume density and molecular gas volume density. Kennicutt (1998; also see Kennicutt 1989) framed the problem in terms of surface densities, yielding the Kennicutt–Schmidt relation: $\Sigma_{\rm SFR} \propto \Sigma_{\rm gas}^{1.4\pm0.15}$.

While a power-law index around 1.4 or 1.5 holds for the molecular gas traced by CO(1–0), a power-law index of unity was found when relating the SFR to the molecular gas traced by HCN(1–0) (Solomon et al. 1992; Gao & Solomon 2004b, hereafter GS04b). This difference in index is interpreted as a consequence of the different critical densities[8] of the molecular tracers used. Having a lower critical density, CO(1–0) traces the global molecular gas content, some of which may not be involved in the star formation process, whereas HCN(1–0) traces denser molecular gas ($n > 10^4$ cm^{-3}) more closely linked to star formation. Since the Solomon et al. (1992) and Gao & Solomon (2004a, hereafter GS04a) observations, several interpretations regarding the linear $L_{\rm IR}$–HCN(1–0) relation in galaxies have been put forth by both observational arguments and numerical models.

For example, by extending the linear relationship between the total infrared luminosity, $L_{\rm IR}[\equiv L(8\text{–}1100\ \mu{\rm m})]$, and HCN(1–0) to Galactic cloud cores, Wu et al. (2005) added to the original GS04b interpretation by framing the relationship in terms of individual star-forming dense-gas "units." As one increases the number of dense star-forming clumps in a galaxy, $L_{\rm IR}$ and HCN(1–0) both increase in lock-step. In this view, the only difference between an extreme starburst galaxy and Galactic star-forming region is the number of dense star-forming units emitting HCN and infrared emission.

Recent observations may challenge the existence of the tight, linear correlation between $L_{\rm IR}$ and HCN(1–0) luminosity[9] reported by GS04b. For instance, Graciá-Carpio et al. (2008, hereafter GC08) obtained new HCN and $\rm HCO^+$ measurements for 17 luminous and ultraluminous infrared galaxies (LIRGs: $10^{11}\ L_\odot < L_{\rm IR} < 10^{12}\ L_\odot$ and ULIRGs: $L_{\rm IR} > 10^{12}\ L_\odot$). They found conflicting HCN(1–0) measurements for several galaxies that overlap with the Solomon et al. (1992) sample. They attribute the differences to calibration errors in the older survey and proceed to compare their revised $L_{\rm IR}$–$L'_{\rm HCN}$ relation with the original one. They find a larger and more significant increase of $L_{\rm IR}$–$L'_{\rm HCN}$ with $L_{\rm IR}$, meaning that the $L_{\rm IR}$–$L'_{\rm HCN}$ power law would be steeper than an index of unity. These authors interpreted the higher $L_{\rm IR}/L'_{\rm HCN}$ ratio as an enhanced star formation efficiency in ULIRGs.

[7] CfA Fellow
[8] $n_{\rm crit} \equiv A_{\rm ul}/\Gamma_{\rm ul}$, where $A_{\rm ul}$ is the Einstein A coefficient and $\Gamma_{\rm ul}$ is the collision rate for a transition from upper (u) to lower (l) energy level.
[9] We use the notation L' for molecular line luminosities as they are expressed in K km s^{-1} pc^2, whereas other luminosities are expressed in $L_\odot$.

A large fraction of nearby LIRGs and ULIRGs appear to be mergers of gas-rich progenitor galaxies and therefore have a high concentration of dense molecular gas in their center which feeds strong starburst and active galactic nucleus (AGN) activity (see Sanders & Mirabel 1996 and references therein). It has been noted that sources with brighter IR luminosities are both more likely to host an AGN (e.g., Veilleux et al. 1995; Lutz et al. 1998; Veilleux et al. 1999), as well as show higher HCN(1–0)/CO(1–0) molecular line luminosity ratios (GS04b; Graciá-Carpio et al. 2006). It is tempting to associate the increased HCN(1–0)/CO(1–0) luminosity ratio with the presence of the AGN. Indeed, GC08 report evidence for an enhanced abundance of HCN in ULIRGs and caution that care must be taken when converting HCN line luminosities into dense gas masses.

Moreover, some theoretical work suggests that AGN-induced processes could potentially increase the abundance of HCN (e.g., Lintott & Viti 2006), causing the observed L_{IR}–L'_{HCN} relation to have a shallower slope than the L_{IR}–L'_{CO} relation. In this picture, X-ray emission resulting from AGNs buried in ULIRGs may enhance the abundance of HCN molecules via an increased availability of free electrons that facilitates combination with ions (e.g., $\mathrm{HCNH}^+ + e^- \rightarrow \mathrm{HCN} + \mathrm{H}$). Some high-resolution HCN observations of nearby galaxies have shown stronger emission of HCN(1–0) relative to CO(1–0) in the center of a few LIRGs and ULIRGs known to host an AGN (e.g., Graciá-Carpio et al. 2006; Krips 2007). These authors have interpreted this higher molecular line ratio in terms of an increased abundance of HCN. Others interpret high molecular line ratios in terms of the mid-plane pressure in the sense that larger ambient pressure could trap or maintain dense gas (Levine et al. 2008; Blitz & Rosolowsky 2006).

In recent years, new theoretical models suggest a different physical explanation for the observed L_{IR}–molecular line luminosity relationships. Specifically, models that couple non-local thermodynamic equilibrium (LTE) radiative transfer calculations with models of star-forming giant molecular clouds (GMCs; Krumholz & Thompson 2007) and hydrodynamic simulations of disk galaxies and galaxy mergers (Narayanan et al. 2008a) find that the driving force controlling the SFR–L_{mol} relation in galaxies is the fraction of thermalized molecular gas at a given molecular transition. In the Krumholz & Thompson (2007) and Narayanan et al. (2008a) picture, the SFR is controlled by the relation SFR $\propto n^{1.5}$, where n is the number density of molecular hydrogen. When the observed molecular line traces the bulk of the molecular gas in the galaxy (e.g., CO(1–0)), the SFR–L_{mol} power-law index (hereafter "slope" as this relationship is typically considered in log–log space) is equivalent to the Kennicutt–Schmidt index (i.e., close to 1.5). On the other hand, higher critical density molecular line tracers (e.g., HCN(1–0)) trace an increasingly smaller fraction of the gas in a galaxy, and so the index in the observed SFR–L_{mol} power-law relation decreases. These theories were tested by Bussmann et al. (2008), who observed HCN(3–2)—a higher critical density tracer than HCN(1–0)—in the GS04a,b samples of galaxies, and found an SFR–HCN(3–2) index less than unity (0.72 ± 0.08).

In this paper, we expand on the Bussmann et al. (2008) work by studying the relationship between five molecular line tracers and infrared luminosity. In particular, we emphasize the importance of considering the critical density of each molecular line tracer. We present support that HCN(1–0) is a valid probe of dense molecular gas, and we revisit the interpretation of the enhanced HCN(1–0)/CO(1–0) luminosity ratio in high IR luminosity systems. Our results suggest that this feature is primarily driven by the increased dense gas fraction in galaxies undergoing a merger and/or a strong episode of starburst activity; we do not require X-ray-driven chemical abundance effects to explain the observed molecular line ratios. Overall, we build a coherent picture where the governing parameter is the density distribution of the molecular gas.

We describe our sample of 34 galaxies in Section 2, along with the measurements that we use. Section 3 contains our results regarding power-law relationships between infrared luminosity and various molecular line luminosities (Section 3.1), as well as the study of molecular line ratios as a function of infrared luminosity (Section 3.2). The interpretation is partially based on the theoretical models of Narayanan et al. (2008a), which we apply to this study in Section 4. We include a brief discussion of chemistry effects in Section 5 and present our conclusions in Section 6. Throughout this paper, we assume a flat ΛCDM cosmological model with $(\Omega_M, \Omega_\Lambda, \mathrm{H}_0) = (0.3, 0.7, 70\ \mathrm{km\ s^{-1}\ Mpc^{-1}})$.

2. METHODS

2.1. Sample

Our primary sample consists of 29 nearby galaxies with HCN(1–0) observations GS04b as well as integrated optical spectroscopy (Moustakas & Kennicutt 2006, hereafter MK06). We obtained follow-up HCN(3–2) observations for 22 of these 29 galaxies (10 detections and 12 upper limits) using the 10 m Heinrich Hertz Submillimeter Telescope (see Bussmann et al. 2008, hereafter B08, for more detail on the HCN(3–2) observations). In order to expand our sample and include additional transitions spanning a range of critical densities and excitation states, we incorporate the sample from GC08. These authors include observations of the HCN(1–0), HCN(3–2), $\mathrm{HCO^+}$(1–0), $\mathrm{HCO^+}$(3–2) transitions for 17 galaxies, of which 12 overlap with our original sample. Thus, the combined sample comprises 34 galaxies. We note a distinction between our primary sample and that of GC08. While the GC08 sample spans the high infrared luminosities ($L_{\mathrm{IR}} = 10^{11.3}$–$10^{12.5}\ L_\odot$), our sample extends the range down to $L_{\mathrm{IR}} \sim 10^{10}\ L_\odot$.

Molecular line and (far-)infrared luminosities are tabulated in Table 1. When combining our primary sample and the GC08 sample, we convert all the luminosities to common cosmological parameters and luminosity distances. The CO(1–0) and HCN(1–0) measurements were taken from GS04a,b. When available, we substitute updated HCN(1–0) luminosities from GC08. These authors published new HCN(1–0) luminosities for their 17 galaxies and found significantly different values for galaxies overlapping with the Solomon et al. (1992) subsample. These galaxies were also included in the GS04b compilation, and the new values from GC08 are approximately a factor of 2 lower in several cases. GC08 attributed these discrepancies to observational errors, namely the calibration of the receiver used on the 30 m IRAM telescope during the earlier observations.

$L'_{\mathrm{HCN(3-2)}}$ values were obtained from B08 (see Appendix) and GC08. Among eight galaxies in common, five have consistent values within the uncertainty, in which case we use the average (or the maximum upper limit in the case of two upper limits). We adopt the GC08 measurements for two non-detections in B08 (Mrk 231 & IRAS 17208-0014), as well as for NGC 6240, which had a discrepant measurement. This galaxy has a very broad HCN(3–2) emission line, so in this case we prefer to use the data from GC08 because of their significantly wider bandwidth.

Table 1
Infrared, Far-infrared, and Molecular Line Luminosities for Our Combined Sample of 34 Galaxies

Source	D_L (Mpc)	$L_{\rm IR}$ $\log(L_\odot)$	$L_{\rm FIR}$ $\log(L_\odot)$	$L'_{\rm CO(1-0)}$ [a] $\log(L')$	$L'_{\rm HCN(1-0)}$ [a] $\log(L')$	$L'_{\rm HCN(3-2)}$ $\log(L')$	$L'_{\rm HCO^+(1-0)}$ $\log(L')$	$L'_{\rm HCO^+(3-2)}$ $\log(L')$	Class
IC 1623	84 ± 6	11.64 ± 0.07	11.48 ± 0.07	10.14 ± 0.10	8.95 ± 0.10	...	...	...	SF
NGC 520	37 ± 3	11.04 ± 0.09	10.93 ± 0.09	9.38 ± 0.10	7.97 ± 0.10	7.15 ± 0.09	...	...	SF/AGN
NGC 660	13 ± 1	10.50 ± 0.11	10.37 ± 0.11	8.80 ± 0.10	>7.35	6.60 ± 0.11	...	...	SF/AGN
NGC 695	135 ± 7	11.62 ± 0.05	11.48 ± 0.05	9.98 ± 0.10	8.29 ± 0.09	<7.75	8.44 ± 0.06	<7.84	SF
NGC 1068	16 ± 1	11.41 ± 0.10	11.04 ± 0.10	9.31 ± 0.10	8.55 ± 0.10	7.58 ± 0.09	...	...	AGN
NGC 1144	119 ± 7	11.39 ± 0.06	11.27 ± 0.06	10.06 ± 0.10	8.45 ± 0.10	...	...	...	SF
NGC 1614	67 ± 5	11.60 ± 0.08	11.40 ± 0.08	9.45 ± 0.10	8.15 ± 0.10	<7.36	...	...	SF/AGN
05189−2524[b]	180 ± 7	12.08 ± 0.04	11.84 ± 0.04	9.87 ± 0.10	8.84 ± 0.10	...	...	...	AGN
NGC 2146	17 ± 2	11.08 ± 0.10	10.93 ± 0.10	9.24 ± 0.10	8.12 ± 0.10	6.41 ± 0.10	...	...	SF/AGN
Arp 55	170 ± 7	11.66 ± 0.04	11.56 ± 0.04	10.14 ± 0.10	8.69 ± 0.04	<8.17	8.65 ± 0.06	8.11 ± 0.12	SF
NGC 2903	8 ± 1	10.23 ± 0.18	10.08 ± 0.18	8.68 ± 0.10	>7.27	5.95 ± 0.10	...	...	SF
UGC 05101	170 ± 7	11.93 ± 0.04	11.84 ± 0.04	9.76 ± 0.10	8.98 ± 0.04	<7.87	8.70 ± 0.07	8.45 ± 0.04	AGN
NGC 3079	19 ± 1	10.76 ± 0.09	10.65 ± 0.09	9.54 ± 0.10	8.16 ± 0.10	7.20 ± 0.08	...	...	SF/AGN
NGC 3628	11 ± 1	10.36 ± 0.09	10.24 ± 0.09	9.24 ± 0.10	7.77 ± 0.10	6.56 ± 0.10	...	...	SF
NGC 3893	15 ± 1	10.14 ± 0.09	10.00 ± 0.09	8.71 ± 0.10	7.46 ± 0.10	<6.00	...	...	SF
NGC 4414	17 ± 0	10.54 ± 0.02	10.40 ± 0.02	9.22 ± 0.10	7.76 ± 0.10	<5.70	...	...	SF
Arp 193	106 ± 7	11.64 ± 0.06	11.55 ± 0.06	9.72 ± 0.10	8.49 ± 0.03	7.88 ± 0.04[d]	8.70 ± 0.03	8.23 ± 0.03	AGN
NGC 5194	8 ± 1	10.33 ± 0.13	10.20 ± 0.13	9.13 ± 0.10	7.54 ± 0.10	...	...	...	SF
UGC 08696	165 ± 7	12.09 ± 0.04	11.98 ± 0.04	9.89 ± 0.10	8.87 ± 0.05	8.56 ± 0.09[e]	8.88 ± 0.05	8.53 ± 0.04	AGN
Arp 220	85 ± 6	12.16 ± 0.07	12.08 ± 0.07	10.01 ± 0.10	9.23 ± 0.01	8.82 ± 0.02[d]	8.89 ± 0.02	8.23 ± 0.02	AGN
NGC 6240	111 ± 7	11.84 ± 0.06	11.69 ± 0.06	10.01 ± 0.10	8.89 ± 0.04	8.78 ± 0.04[e]	9.15 ± 0.02	8.45 ± 0.06	AGN
17208-0014[b]	187 ± 7	12.32 ± 0.04	12.25 ± 0.04	10.24 ± 0.10	9.27 ± 0.03	8.87 ± 0.04[e]	9.10 ± 0.04	8.67 ± 0.05	SF
NGC 6701	61 ± 5	11.07 ± 0.08	10.94 ± 0.08	9.59 ± 0.10	8.20 ± 0.10	7.43 ± 0.13	...	...	SF/AGN
NGC 7130	71 ± 6	11.35 ± 0.07	11.22 ± 0.07	9.73 ± 0.10	8.59 ± 0.10	...	...	...	SF/AGN
IC 5179	50 ± 4	11.18 ± 0.08	11.05 ± 0.08	9.49 ± 0.10	8.61 ± 0.10	...	...	...	SF
NGC 7469	69 ± 2	11.59 ± 0.04	11.39 ± 0.04	9.59 ± 0.10	8.43 ± 0.02	7.87 ± 0.05[d]	8.59 ± 0.01	7.79 ± 0.09	AGN
23365+3604[b]	269 ± 6	12.12 ± 0.02	11.97 ± 0.02	9.94 ± 0.10	8.78 ± 0.08	<8.47[f]	8.61 ± 0.10	...	AGN
NGC 7771	60 ± 5	11.35 ± 0.08	11.23 ± 0.08	9.96 ± 0.10	8.63 ± 0.01	7.85 ± 0.03[d]	8.62 ± 0.03	7.67 ± 0.08	SF
Mrk 331	77 ± 6	11.42 ± 0.07	11.28 ± 0.07	9.75 ± 0.10	8.41 ± 0.02	7.66 ± 0.10[e]	8.50 ± 0.02	7.94 ± 0.07	SF/AGN
Mrk 231[c]	188	12.51 ± 0.07	12.26 ± 0.07	10.00 ± 0.10	9.09 ± 0.03	8.49 ± 0.05[e]	9.07 ± 0.04	8.50 ± 0.06	AGN
12112+0305[b,c]	335	12.31 ± 0.07	12.19 ± 0.07	...	9.22 ± 0.09	<8.90[e]	8.99 ± 0.11	...	AGN
VII Zw 31[c]	241	11.96 ± 0.07	11.83 ± 0.07	10.16 ± 0.10	8.84 ± 0.07	<8.57	8.90 ± 0.06	8.44 ± 0.10	SF
Arp 299A[c]	50 ± 4	11.67 ± 0.07	11.48 ± 0.07	...	8.21 ± 0.02	7.45 ± 0.11[e]	8.48 ± 0.02	7.93 ± 0.04	SF/AGN
Arp 299B[c]	50 ± 4	11.56 ± 0.07	11.29 ± 0.07	...	8.02 ± 0.03	<7.19[e]	8.22 ± 0.03	7.55 ± 0.07	SF/AGN

Notes. The optical classification is included in the last column.
[a] When no formal uncertainties are available for published CO(1–0) or HCN(1–0) line luminosities, we estimate the calibration error to be 0.1 dex (20%–25%).
[b] Full galaxy name starts with IRAS.
[c] These five galaxies are not part of our primary sample. $L_{\rm IR}$ and $L_{\rm FIR}$ were obtained from GC08 after converting their luminosity distance to our assumed cosmology ($\{\Omega_M, \Omega_\Lambda, H_0\} = \{0.3, 0.7, 70\ \rm km\ s^{-1}\ Mpc^{-1}\}$). Because GC08 do not provide errors on $L_{\rm IR}$ and $L_{\rm FIR}$, we use the mean error for the rest of our sample (≈ 0.07 dex).
[d] Average of B08 and GC08 values.
[e] Measurement from GC08.
[f] Upper limit in both B08 and GC08 surveys.

A few galaxies in our sample were also observed by Krips et al. (2008). These authors report brighter HCN(3–2) for five overlapping galaxies, most notably for the most IR-luminous galaxies (e.g., Mrk 231). To maintain homogeneity in our selected set of observations, and to facilitate the comparison with the work of GC08, we restrict our analysis to the HCN(3–2) luminosities from B08 and GC08. However, we anticipate that including the few higher values from Krips et al. (2008) would either strengthen the trends presented in Section 3 or leave them unchanged.

We use the $L'_{\rm HCO^+(1-0)}$ and $L'_{\rm HCO^+(3-2)}$ measurements published in GC08 with a conversion for the luminosity distances adopted here. On average, this distance conversion changes molecular line luminosities by 0.055 dex (min = −0.073 and max = 0.16), which is less than the average uncertainty on these quantities.

Observing different molecular transitions with a variety of telescopes leads to varying beam sizes. Since most sources in the samples we use in this study have not been mapped, it is important to consider aperture affects associated with the use of varying beam sizes. First, two galaxies have a lower limit in HCN(1–0) because they were not mapped even though they are nearby (NGC 660 and NGC 2903; see GS04a). For the HCN(3–2) observations in B08, the beam size of 30″ is sufficient to cover the central kpc for galaxies beyond 7 Mpc. We expect to detect most of the HCN(3–2) emission in these cases since it is the dense nuclear regions of galaxies that are responsible for the majority of the emission from molecular transitions with high critical densities for excitation. Meanwhile, targets selected for study in GC08 all lie at distances >60 Mpc and, therefore, we are assured of sampling the full extent of the high-density molecular emission.

2.2. Optical AGN Classification

The nature of the powering source of galaxies in our sample (star formation, AGNs, or hybrid, i.e., hosting both star

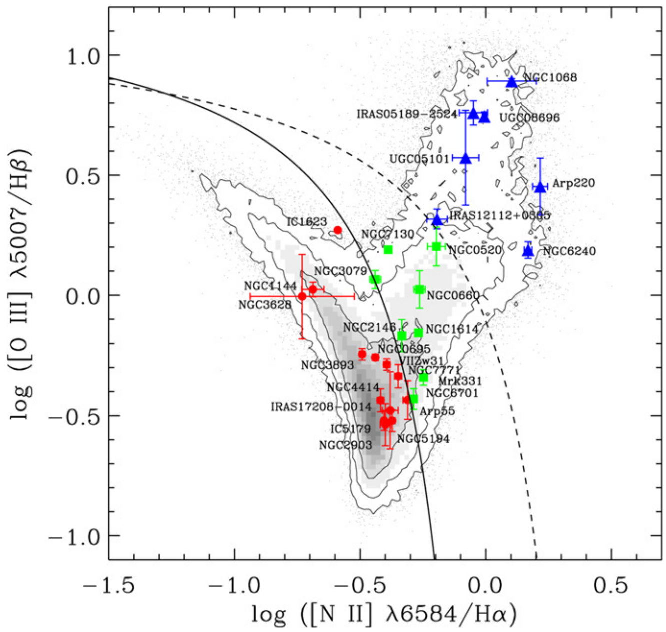

Figure 1. Emission-line diagnostic diagram indicating the position of normal star-forming galaxies (below and to the left of the solid curve), AGNs (above and to the right of the dashed curve), and galaxies with an admixture of star formation and AGN activity (between the solid and dashed curves). The individual galaxies in our sample are labeled and plotted using color symbols with error bars, with the exception of five galaxies mentioned in the text. The different symbols represent the optical spectral type: star-forming (SF; red circles); AGN (blue triangles); and SF/AGN (green squares). For reference, the gray-scale and contours (enclosing 52%, 84%, and 97% of the points) show the locus of emission-line galaxies in the SDSS. The solid and dashed curves are adapted from Kauffmann (2003) and Kewley et al. (2001), respectively.

(A color version of this figure is available in the online journal.)

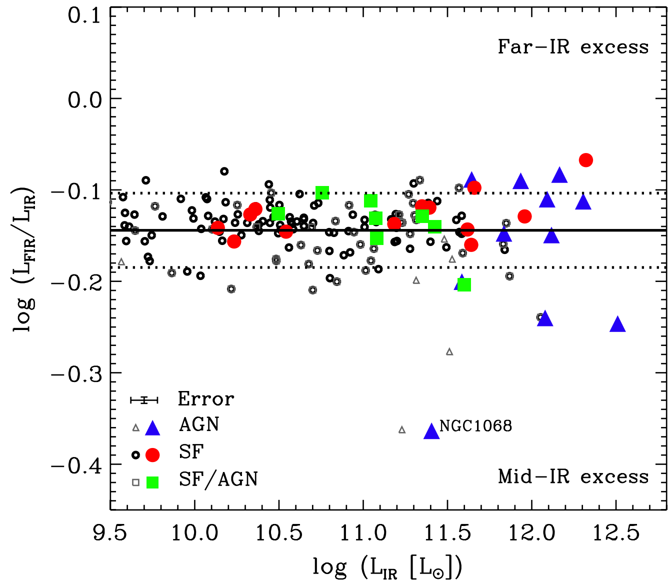

Figure 2. FIR/IR luminosity ratio for the MK06 sample of galaxies (gray and black open symbols) and for our combined sample of galaxies (filled colored symbols as in Figure 1; also see legend). We find an average value of $\log(L_{FIR}/L_{IR}) = -0.14$ (corresponding to $L_{IR}/L_{FIR} = 1.38$, which is close to the value of 1.3 used in GC08). Although most of the galaxies in our sample are fairly close to that value, there are some noticeable outliers, the most striking one being NGC 1068. We stress that our results remain unchanged (within the uncertainties) if we adopt FIR instead of total IR luminosities in our analysis.

(A color version of this figure is available in the online journal.)

formation and AGN activity) is determined using the optical diagnostic diagram known as the BPT diagram (Baldwin et al. 1981; Veilleux & Osterbrock 1987; Osterbrock 1989). The optical emission-line ratios used in this diagram ([O III] λ5007/Hβ and [N II] λ6584/Hα) probe a combination of the oxygen abundance and ionization parameter of the interstellar medium (ISM) present in these galaxies. This provides us with an indirect signature of the source of ionizing radiation (young stars versus AGNs). As shown in Figure 1, the Sloan Digital Sky Survey (SDSS; York et al. 2000) galaxies (gray area and contours) show a tight excitation sequence of star-forming galaxies (below the solid line from Kauffmann 2003), as well as a plume of galaxies that are either hybrid (between the solid and dashed lines) or AGNs (above the dashed line adapted from Kewley et al. 2001). The SDSS emission-line measurements are taken from the MPA/JHU SDSS team Web site[10] (Brinchmann et al. 2004; Tremonti et al. 2004) based on observations of galaxies contained in the SDSS data release 7 (DR7; Abazajian et al. 2009).

Galaxies from our combined sample are overlaid with colored symbols. Among 34 galaxies, 13 are classified as star-forming (SF, red circles), 10 galaxies are classified as hybrid (SF/AGNs, green squares), and 11 galaxies show a strong signature of AGNs (blue triangles). These numbers include five galaxies that are classified but not shown in the diagram. Two galaxies (Mrk 231 and NGC 7469) have obvious broad emission lines in their optical spectrum indicating a type 1 (broad-line) AGNs, and therefore need not be classified using this narrow-line diagnostic. IRAS 23365+3604 fails the signal-to-noise cut for the [N II] λ6584 line but occupies the AGN portion of the [O I]λ6300/Hα diagram. Finally, Arp 299A and Arp 299B are both classified as SF/AGNs based on the classification of the Arp 299 system. With the exception of IRAS 12112+0305 and VII Zw 31, spectra were obtained with a long-slit drift-scanning technique in order to integrate the light spatially (MK06). Spectroscopic measurements for IRAS 12112+0305 and VII Zw 31 were obtained from Veilleux et al. (1999) and Wu et al. (1998), respectively.

We note that dust obscuration can challenge the identification of an AGN in the optical spectral range. Sufficient optically thick material with a large covering fraction surrounding the nuclear region could potentially mask all AGN signatures at these wavelengths. However, we identify an AGN in all but one of the most IR-bright galaxies (IRAS 17208–0014). The latter is the only optically obscured, potentially MIR-obscured, AGN candidate sometimes referred to as the *buried AGN* (Imanishi 2009). We also note that although this diagnostic indicates the presence of an AGN, it does not allow us to quantify its strength and its relative contribution to the total infrared light of its host galaxy. For example, the well-known ULIRG Arp 220 is thought to be mainly powered by star formation (Lutz et al. 1996) even though it is known to host a Seyfert nucleus (Rieke et al. 1985). Furthermore, there has been accumulating evidence that most LIRGs and ULIRGs are mainly powered by starbursts (Lutz et al. 1998; Genzel et al. 1998; Farrah et al. 2003; Vega et al. 2008; Nardini et al. 2008), except for a few notable cases such as Mrk 231 (Condon et al. 1991; Spoon et al. 2007), IRAS 05189−2524 (Spoon et al. 2007; Armus et al. 2007), and NGC 1068 (Le Floc'h et al. 2001). These three examples stand out from the rest of our sample as they exhibit the largest mid-IR excesses (they correspond to the three blue triangles below the dotted line in Figure 2).

Among others, Nardini et al. (2008) report that the AGN contribution may dominate in the mid-IR range while remaining

[10] http://www.mpa-garching.mpg.de/SDSS/DR7

Table 2
Slopes of $\log(L_{IR})-\log(L'_{mol})$ and $\log(L_{FIR})-\log(L'_{mol})$ for Five Molecular Lines

Transition	$\log(n_{crit}[cm^{-3}])$	β_{IR}	β_{FIR}	$\beta_{FIR}-\beta_{IR}$	Sample
CO(J = 1–0)	3.3	1.30 ± 0.17	1.34 ± 0.16	0.04	Combined
HCO^+(J = 1–0)	5.3	0.99 ± 0.26	1.07 ± 0.26	0.08	GC08
HCN(J = 1–0)	6.5	1.13 ± 0.11	1.14 ± 0.10	0.01	Combined
HCO^+(J = 3–2)	6.6	0.81 ± 0.21	0.90 ± 0.19	0.09	GC08
HCN(J = 3–2)	7.7	0.70 ± 0.09	0.71 ± 0.08	0.01	Combined

Note. The transitions are ordered in increasing critical density (n_{crit}). For each transition, we report the difference between the two values of slopes ($\beta_{FIR}-\beta_{IR}$) and we identify the sample used for the calculations.

Table 3
Slopes of $\log(L'_{HD}/L'_{LD})-\log(L_{IR})$ and $\log(L'_{HD}/L'_{LD})-\log(L_{FIR})$ for Ten Molecular Line Luminosity Ratios

Line Ratio	R_{crit}	α_{IR}	α_{FIR}	r_{IR}	r_{FIR}
HCO^+_{3-2}/HCN_{1-0}	0.1	−0.054 ± 0.24	−0.068 ± 0.22	−0.05	−0.08
HCN_{1-0}/HCO^+_{1-0}	1.1	0.32 ± 0.15	0.36 ± 0.13	0.60	0.66
HCN_{3-2}/HCO^+_{3-2}	1.2	0.32 ± 0.39	0.38 ± 0.38	0.37	0.42
HCO^+_{3-2}/HCO^+_{1-0}	1.3	0.24 ± 0.17	0.26 ± 0.15	0.48	0.53
HCN_{3-2}/HCN_{1-0}	1.3	0.41 ± 0.11	0.41 ± 0.12	0.70	0.72
HCO^+_{1-0}/CO_{1-0}	2.0	0.24 ± 0.20	0.22 ± 0.19	0.40	0.28
HCN_{3-2}/HCO^+_{1-0}	2.4	0.53 ± 0.31	0.62 ± 0.30	0.68	0.75
HCN_{1-0}/CO_{1-0}	3.1	0.23 ± 0.064	0.22 ± 0.065	0.53	0.49
HCO^+_{3-2}/CO_{1-0}	3.2	0.48 ± 0.27	0.48 ± 0.26	0.60	0.60
HCN_{3-2}/CO_{1-0}	4.4	0.70 ± 0.12	0.68 ± 0.11	0.87	0.87

Note. For each line ratio, we report the contrast in critical density (R_{crit}), the mean and standard deviations of the slope distributions (α_{IR} & α_{FIR}), and the linear correlation coefficients (r_{IR} & r_{FIR}).

a small fraction of the total infrared light, typically less than 25%. Recent work suggests a correlation between the optical spectral classification and the AGN contribution to the bolometric luminosity of ULIRGs. Using a sample of 74 ULIRGs, Veilleux et al. (2009) find that the AGN contribution ranges from ∼15% to 35% among purely SF and LINER ULIRGs to ∼50 and 75% among Seyfert 2 and Seyfert 1 ULIRGs, respectively. Individual galaxies may deviate from this trend as their sample includes a Seyfert 2 ULIRG with as little as 20% AGN contribution and SF-classified ULIRGs with roughly 50% AGN contribution. Thus, we stress that although the optical classification used here indicates the presence of an AGN, it does not allow us to quantify its contribution at infrared wavelengths on a galaxy-by-galaxy basis. Indeed, several systems classified as AGNs are also undergoing major episodes of star formation.

2.3. Infrared Luminosity

We estimate far-infrared [$L_{FIR} \equiv L(40\text{–}500\ \mu m)$] and total infrared [$L_{IR} \equiv L(8\text{–}1100\ \mu m)$] luminosities of the galaxies in our sample using *IRAS* observations at 12, 25, 60, and 100 μm (Sanders et al. 2003). Following Moustakas et al. (2006), we model the infrared spectral energy distribution (SED) of each object longward of 100 μm using a modified blackbody with dust emissivity proportional to λ^{-1} and dust temperature given by the observed $S_\nu(60\ \mu m)/S_\nu(100\ \mu m)$ flux ratio (Gordon et al. 2000; Bell 2003). We then integrate numerically over the appropriate wavelength range to derive L_{FIR} and L_{IR}.

When interpreting galaxy infrared luminosity, one has to take into account potential contributions of recent or ongoing star formation, older stellar populations, and AGN activity. In the case of LIRGs and ULIRGs, the infrared emission from dust heated by powerful starbursts dominates over that contributed by old stars, so we ignore the older stellar population component. It has been suggested that because the typical AGN IR SED peaks in the mid-infrared range (around λ = 10–20 μm; e.g., Elvis et al. 1994), the far-infrared portion of the SED roughly corresponds to the star-forming component. We compare the total IR and FIR emission in Figure 2 and find a similar ratio (L_{IR}/L_{FIR} = 1.38) to that reported in the literature (1.3, GC08). Most of the galaxies in our sample lie within 1σ of the mean value obtained for a control sample of galaxies (MK06, small plotting symbols in Figure 2). There are a few outliers, the most striking example being the prototype Seyfert 2 galaxy NGC 1068, which has the largest MIR-excess and lies 4.5σ from the mean. Interestingly, even when the fractional AGN contribution to the mid-IR light dominates over the starburst contribution, it still appears to be the case that the AGN's total IR contribution is mostly less than 25%–30% (Nardini et al. 2008).

The larger spread in L_{IR}/L_{FIR} ratios observed in brighter galaxies may be related to a combination of varying extinction and AGN contribution. For instance, Veilleux et al. (2009) suggest an evolutionary sequence with three AGN classes for nearby ULIRGs. The first class is characterized by small extinctions and large polycyclic aromatic hydrocarbon (PAH) equivalent widths. ULIRGs in this class are highly starburst-dominated. The second class includes galaxies with large extinctions but that are still likely dominated by starburst, while galaxies belonging in the third class show both small extinctions and PAH equivalent widths and have a significant AGN contribution (at least as important as the starburst). A detailed analysis is beyond the scope of this paper, but we refer the reader to published analyses utilizing mid-infrared spectroscopy (e.g., Lutz et al. 1998; Genzel et al. 1998; Spoon et al. 2007; Armus et al. 2007; Farrah et al. 2007). Here, we simply identify the presence of an AGN using optical emission lines (Section 2.2), and we do not attempt to quantify its contribution, given the large uncertainties in doing so.

Because we do not interpret L_{IR} strictly as an SFR, we choose to plot the total infrared luminosity throughout this paper. We repeated our analysis using FIR instead of IR luminosity. This change has a negligible effect on our results (the differences are all well within the uncertainties; see Tables 2 and 3).

2.4. *Numerical Models*

We utilize the numerical models of Narayanan et al. (2008a) as a comparison for our observations. We refer the reader to this work for details on the models, though we summarize the aspects most relevant to the present study.

In an effort to model the observed SFR–L_{mol} relations in galaxies, Narayanan et al. (2008a) coupled three-dimensional non-LTE radiative transfer calculations with smoothed particle hydrodynamics (SPH) simulations of galaxies in evolution. The SPH simulations were calculated utilizing a modified version of the publicly available code GADGET-2 (Springel 2005), including prescriptions for a multi-phase ISM, supernovae pressurization of the ISM, and star-formation following a generalized (three-dimensional) version of the Kennicutt–Schmidt law (Springel & Hernquist 2003). Here, we set the index of the Kennicutt–Schmidt relation to 1.5, which has important consequences in driving the simulated SFR–L_{mol} relations (Narayanan et al. 2008a). We additionally include energy feedback from accreting AGNs (Springel et al. 2005), though note that it has negligible impact on the simulated SFR–L_{mol} relations.

The molecular line emission properties of the model galaxies were extracted using the three-dimensional non-LTE radiative transfer code, *Turtlebeach* (Narayanan et al. 2006). *Turtlebeach* considers both collisional and radiative (de-)excitation in determining the level populations of a given molecule, and utilizes Monte Carlo methods for sampling the spatial and frequency domains. Because the hydrodynamic simulations typically have a coarser physical resolution than the scale of GMCs, sub-grid prescriptions for including GMCs as singular isothermal spheres following a Galactic mass spectrum and mass–radius relation have been implemented (for details, please see Narayanan et al. 2006, 2008b).

The SPH simulations consist of ∼100 galaxies comprised of isolated disks as well as gas-rich, binary, 1:1 galaxy mergers. The structures of the galaxies were initialized following the Mo et al. (1998) formalism. In order to probe a relatively large dynamic range of galaxies, the galaxies were initialized with gas fractions f_g[0.2,0.4,0.8] and total (halo) mass ranging from $\sim 1 \times 10^{12}\ M_\odot$ to $\sim 4 \times 10^{13}\ M_\odot$ spaced in four mass bins. The galaxy mergers were run at a single initial gas fraction and mass ($f_g = 0.4$ and $M_{\mathrm{DM}} = 1 \times 10^{12}\ M_\odot$). A key feature of these simulations is that they include constant Galactic abundances for HCN and CO, i.e., no chemistry is modeled. These simulations were shown to accurately recover the observed L_{IR}–HCN(1–0), L_{IR}–CO(1–0), and L_{IR}–CO(3–2) relations. Furthermore, they predicted a sub-linear L_{IR}–HCN(3–2) relation, which was subsequently observed by B08. The HCN and CO simulations were taken from the study of Narayanan et al. (2008a), while HCO^+ simulations of gas-rich galaxy mergers were run specifically for this work.

3. RESULTS

3.1. *Correlation Between Molecular Line and Infrared Luminosities*

The molecular gas tracers used in this work span a broad range of critical densities ($n_{\mathrm{crit}} \equiv A_{\mathrm{ul}}/\Gamma_{\mathrm{ul}}$) varying between $\sim 10^{3.3}$ cm^{-3} for CO(1–0) and $\sim 10^{7.7}$ cm^{-3} for HCN(3–2) (Figure 3). Although the critical density of HCN(1–0) is an order of magnitude larger than that of HCO^+(1–0), it is almost a perfect match to the critical density of HCO^+(3–2). In what follows, we consider the values of n_{crit} at an assumed temperature of 30 K, noting that they are roughly constant over a broad range of temperatures (20–100 K; see Figure 3). Even though we use n_{crit} to guide some of our interpretations, we caution that molecular gas emission can be observed in gas with densities less than critical (Evans 1999). Substituting critical densities with effective densities as defined in Evans (1999) does not alter our main conclusions.

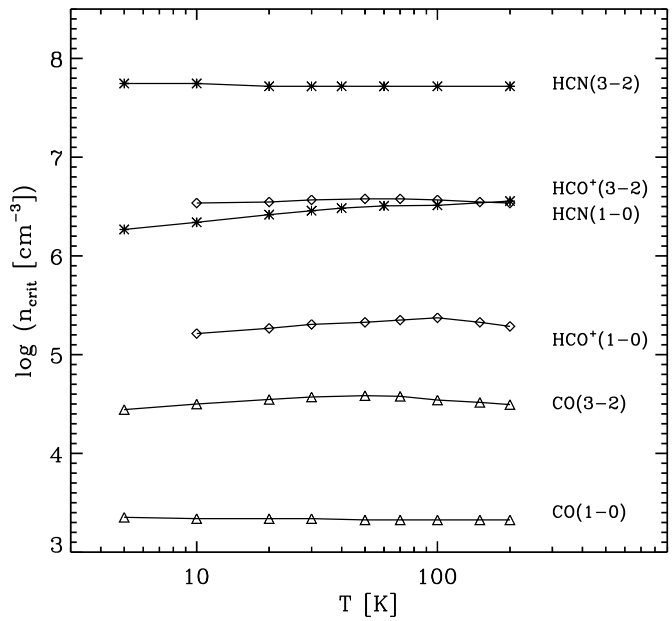

Figure 3. Critical density, $n_{\mathrm{crit}} \equiv A_{\mathrm{ul}}/\Gamma_{\mathrm{ul}}$, for typical molecular transitions used to trace molecular gas in galaxies. The critical density is fairly insensitive to temperature over a wide range. Note that the HCN(1–0) and HCO^+(3–2) transitions have a remarkably close value of critical density, whereas the critical density of HCO^+(1–0) is over one order of magnitude smaller than that of HCN(1–0). Molecular data come from the Leiden Atomic and Molecular Database (Schöier et al. 2005).

Assuming that L_{IR} (or L_{FIR}) provides a good estimate of the SFR and that the molecular line luminosity traces the mass of molecular gas above a certain density, L_{IR}–L'_{mol} relations (or their surface density equivalent) are commonly interpreted and/or used to derive universal SFR prescriptions. In this section, we present relationships between galaxy infrared luminosity and the luminosity of various molecular lines. We compute the slope (β) between log(L_{IR}) and the molecular line luminosity of CO(1–0), HCO^+(1–0), HCO^+(3–2), HCN(1–0), and HCN(3–2) (Figure 4). When available, we compute the slope for the combined sample (solid lines). However, observations for the HCO^+(1–0) and HCO^+(3–2) transitions are only available for the GC08 sample (open symbols). The latter sample comprises fewer galaxies and is biased toward higher infrared luminosities, resulting in derived slopes (dashed lines) with much larger uncertainties. Galaxies hosting an AGN (blue triangles) occupy the bright end of L_{IR} but appear to follow the same relationship as the rest of the sample. Molecular line non-detections are shown with arrows but are not included when computing the slope (β) or the Pearson correlation coefficient (r).

All slopes are computed using the LINMIX IDL routines from Kelly (2007). In these routines, the distributions of independent variables are modeled as a mixture of Gaussian functions, which allows for greater flexibility when computing the true distributions of these variables (i.e., without measurement errors) given the observations. Using a Bayesian statistical approach, the likelihood distribution function is computed and then integrated over the entire data set. This method offers

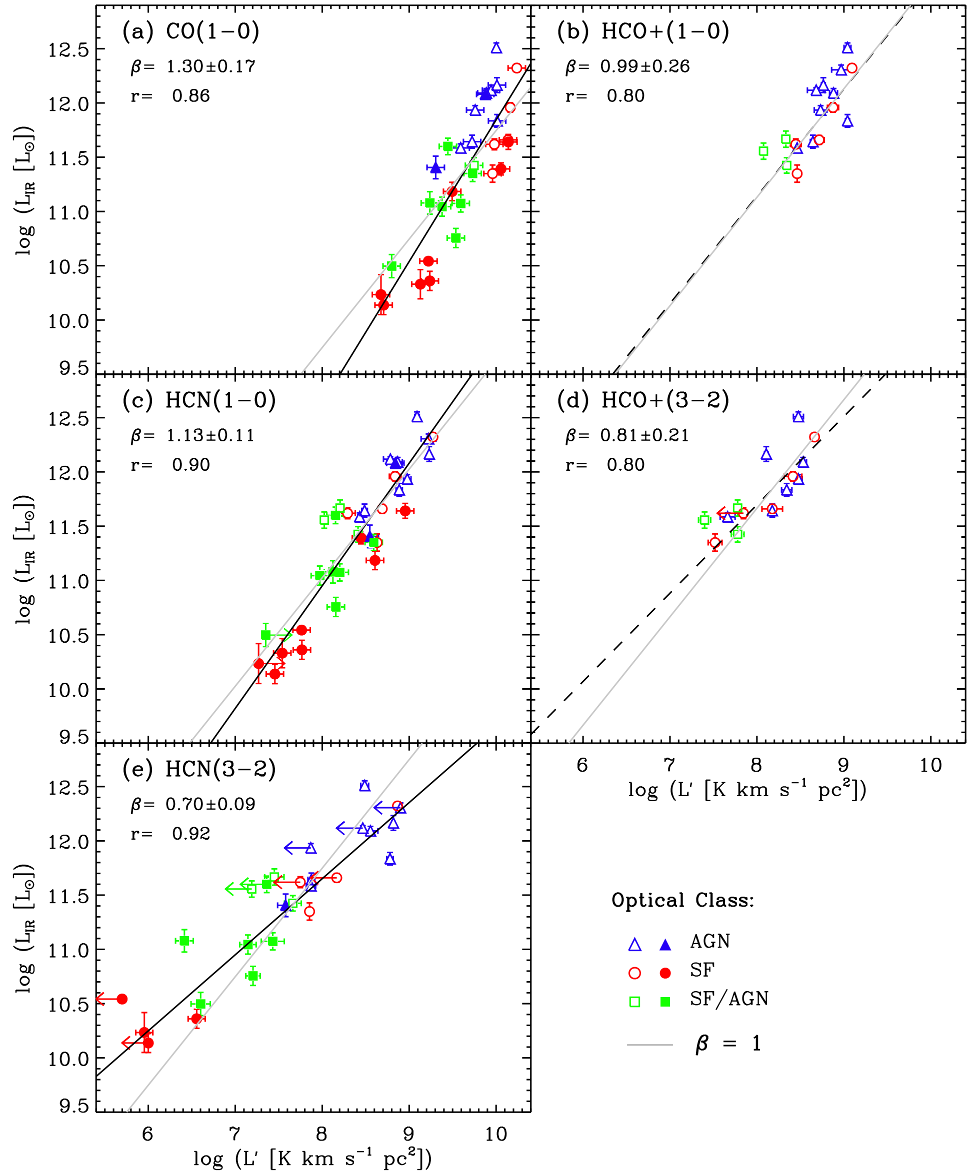

Figure 4. Relationship between infrared luminosity and CO(1–0) (a), HCO$^+$(1–0) (b), HCN(1–0) (c), HCO$^+$(3–2) (d), and HCN(3–2) (e), molecular line luminosities. We show galaxies from our primary sample (filled symbols) as well as from the GC08 sample (open symbols). Panels are ordered by increasing molecular line critical density. Our optical AGN classification is shown using the same color scheme as in Figure 1 (also see legend). Each panel is labeled with the mean and standard deviation of the corresponding slope (β) distribution and with the linear correlation coefficient r. The gray lines have a slope of unity and are included for visualization purposes.

(A color version of this figure is available in the online journal.)

several advantages compared to other algorithms. Namely, it provides likelihood distributions for the values of slopes and intercepts while allowing for intrinsic scatter (i.e., scatter present in the absence of measurement errors). Most relevant for this work, this method is successful at recovering linear regressions when measurement errors dominate the scatter and when there is a non-negligible number of non-detections in the sample. We note that the value of the slope found using a simple linear least-squares-fitting routine available in IDL (LINFIT) is always included within 1σ of the mean of the distribution of slopes derived by LINMIX. The mean values of the distribution of slopes are shown in Figure 4. We also report the slopes obtained by substituting $L_{\rm IR}$ by $L_{\rm FIR}$ (Table 2). The FIR slopes are slightly higher on average, but consistent within 1σ. Our results agree with previous work in that $\beta_{\rm CO(1-0)} > 1$ (2σ) and that $\beta_{\rm HCN(3-2)} < 1$ (3σ). The derived slopes for HCO$^+$(1–0), HCN(1–0), and HCO$^+$(3–2) are statistically consistent with each other (and with a slope of unity), given the large uncertainties.

Figure 4 suggests that the proportionality between infrared luminosity $\log(L_{\rm IR})$ and molecular line luminosity $\log(L')$ varies as a function of critical density. We compile the mean and standard deviation of slope distributions ($\beta \pm \sigma$) obtained previously and show them as a function of the critical density of the corresponding molecular transition (Figure 5). We find evidence for a shallower $\log(L_{\rm IR})$–$\log(L')$ slope with increasing molecular line critical density. We supplement our results with published relations between $\log(L_{\rm IR})$ and $\log(L'_{\rm mol})$ for the following transitions: CO(1–0) and HCN(1–0) from GS04 (open squares), CO(3–2) from Narayanan et al. (2005, filled circle) and, in order of increasing critical density, CO(1–0), CO(2–1), HCO$^+$(1–0), CS(3–2), and HCN(1–0) from Baan et al. (2008,

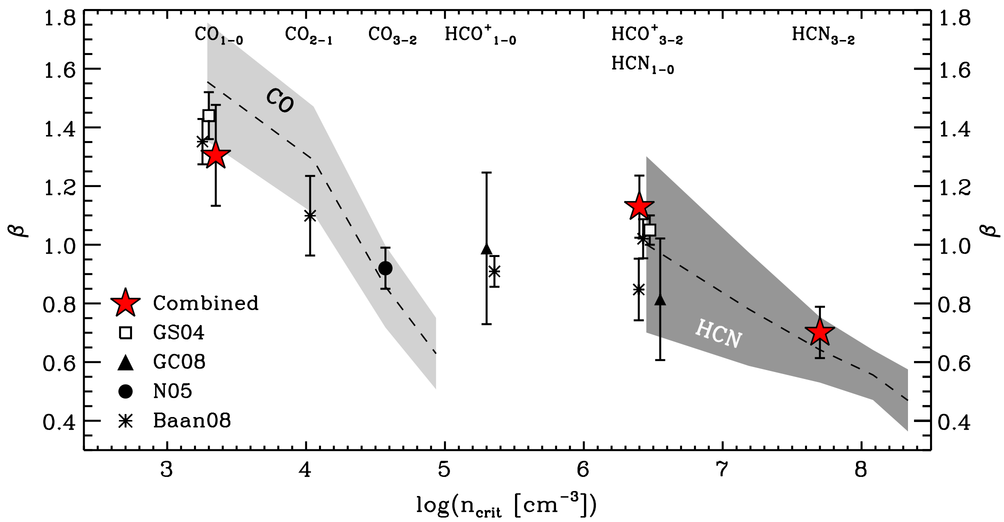

Figure 5. Slope of $\log(L_{\rm IR})-\log(L')$ versus molecular line critical densities for the GC08 sample (triangles) and our combined sample (stars). Individual slopes are shown in the previous figure. We add values from the literature: CO(1–0) and HCN(1–0) from GS04 (open squares), CO(3–2) from Narayanan et al. (2005, filled circle) and, in order of increasing critical density, CO(1–0), CO(2–1), HCO+(1–0), CS(3–2), and HCN(1–0) from Baan et al. (2008, asterisk symbols). The corresponding molecular line transitions are labeled at the top of the figure. Some of the points around $\log(n_{\rm crit})\sim 3.3$ and 6.5 were offset slightly in critical density for clarity of the plotting symbols. The shaded regions show the predictions of N08 models for CO (pale gray), and HCN (dark gray) rotational transitions from $J=1$–0 to $J=5$–4. See the text for more detail.

(A color version of this figure is available in the online journal.)

asterisk symbols). Baan et al. (2008) published slopes for the inverse relation $[\log(L'_{\rm mol})-\log(L_{\rm IR})]$. Thus, the asterisk symbols are not truly calculated slopes, but rather the inverse of the published numbers. These points are included for visual reference, but should be considered more uncertain than the associated error bars. All transitions are labeled at the top of the figure. Points corresponding to HCN(1–0) and HCO+(3–2) are very close given their near-identical critical densities. We added small offsets in critical density for clarity of the plotting symbols around $\log(n_{\rm crit})\sim 3.3$ and 6.5.

Similar results have been found by Iono et al. (2009). These authors looked at the reciprocal relation but find a slope that varies with critical density in the same sense (i.e., the inverse of their slope decreases with $n_{\rm crit}$, reaching close to unity for their higher density tracers). While they only considered CO(1–0), CO(3–2), and HCN(1–0), here we extend the trend to a larger number of molecular line transitions and, more importantly, to a transition with a higher critical density probing the regime where the $\log(L_{\rm IR})$–$\log(L')$ slope is less than unity [HCN(3–2)].

In their coupling of non-LTE radiative transfer calculations with hydrodynamic galaxy evolution simulations, Narayanan et al. (2008a) predicted the SFR–$L_{\rm mol}$ relations in local galaxies as a function of increasing molecular transition which serve as a natural comparison for the observations compiled here. We compare the observations with the numerical simulations of Narayanan and *collaborators* in Figure 5 by overplotting their model predictions as the gray-shaded regions.[11] The predicted slopes were calculated by randomly sampling 25 of the ∼100 model galaxies in the Narayanan et al. (2008a) sample, and calculating the slope for the subset of galaxies. The shaded region is the 1σ dispersion in slopes, and the dashed line is the mean. The model SFR–$L_{\rm mol}$ slope decreases as a function of increasing critical density owing to the arguments described in Section 1. Because higher J-level molecular line transitions trace a smaller fraction of the galaxy's molecular content, the SFR–$L_{\rm mol}$ slope decreases from the assumed Kennicutt–Schmidt index of 1.5. We find good agreement between the compiled molecular line observations and the theoretical predictions for CO and HCN.

3.2. *Comparison Between High- and Low-density Molecular Tracers*

In this section, we study the possibility that the enhanced HCN(1–0)/CO(1–0) luminosity ratio actually corresponds to an enhanced dense gas fraction. The five transitions studied in this work allow us to examine 10 molecular line luminosity ratios as a function of IR luminosity. This set includes published line ratios for which the lines involved probe different densities. We introduce a new line ratio, $L'_{\rm HCO^+(3-2)}/L'_{\rm HCN(1-0)}$, for which both molecular transitions have nearly the same critical density (see Figure 3).

When comparing two tracers, we adopt the convention of dividing the higher density (HD) tracer by the lower density (LD) tracer. We quantify the contrast of their critical densities as follows: $R_{\rm crit}\equiv\log(n^{\rm HD}_{\rm crit}/n^{\rm LD}_{\rm crit})$. Our set of line ratios spans four orders of magnitude in critical density contrast $0.1 < R_{\rm crit} < 4.4$. We quantify the IR luminosity dependence of each molecular line ratio by a power law (see Figure 6). Whenever possible, we fit for our combined sample (open and filled symbols, solid lines). Otherwise, we fit to the GC08 sample only (open symbols, dashed lines). We report the mean and standard deviation on the distribution of possible slopes (α) at the top of each panel. We also include the critical density contrast ($R_{\rm crit}$) and the Pearson linear correlation coefficient (r) in each case.

Our results are summarized in Table 3 and indicate an enhancement in molecular luminosity ratio of high- to low-density tracer ($L'_{\rm HD}/L'_{\rm LD}$) with increasing IR luminosity. This trend is observed, with varying degree of significance, for all ratios with $R_{\rm crit} > 1$. In contrast, $L'_{\rm HCO^+(3-2)}/L'_{\rm HCN(1-0)}$—the only ratio of lines with nearly equal critical densities ($R_{\rm crit}\sim 0$)—remains flat even at high infrared luminosities. The same trend is observed when substituting $L_{\rm IR}$ by $L_{\rm FIR}$ (see Table 3).

[11] We note that Narayanan et al. (2008a) only published the model SFR–$L_{\rm mol}$ slopes for CO and HCN.

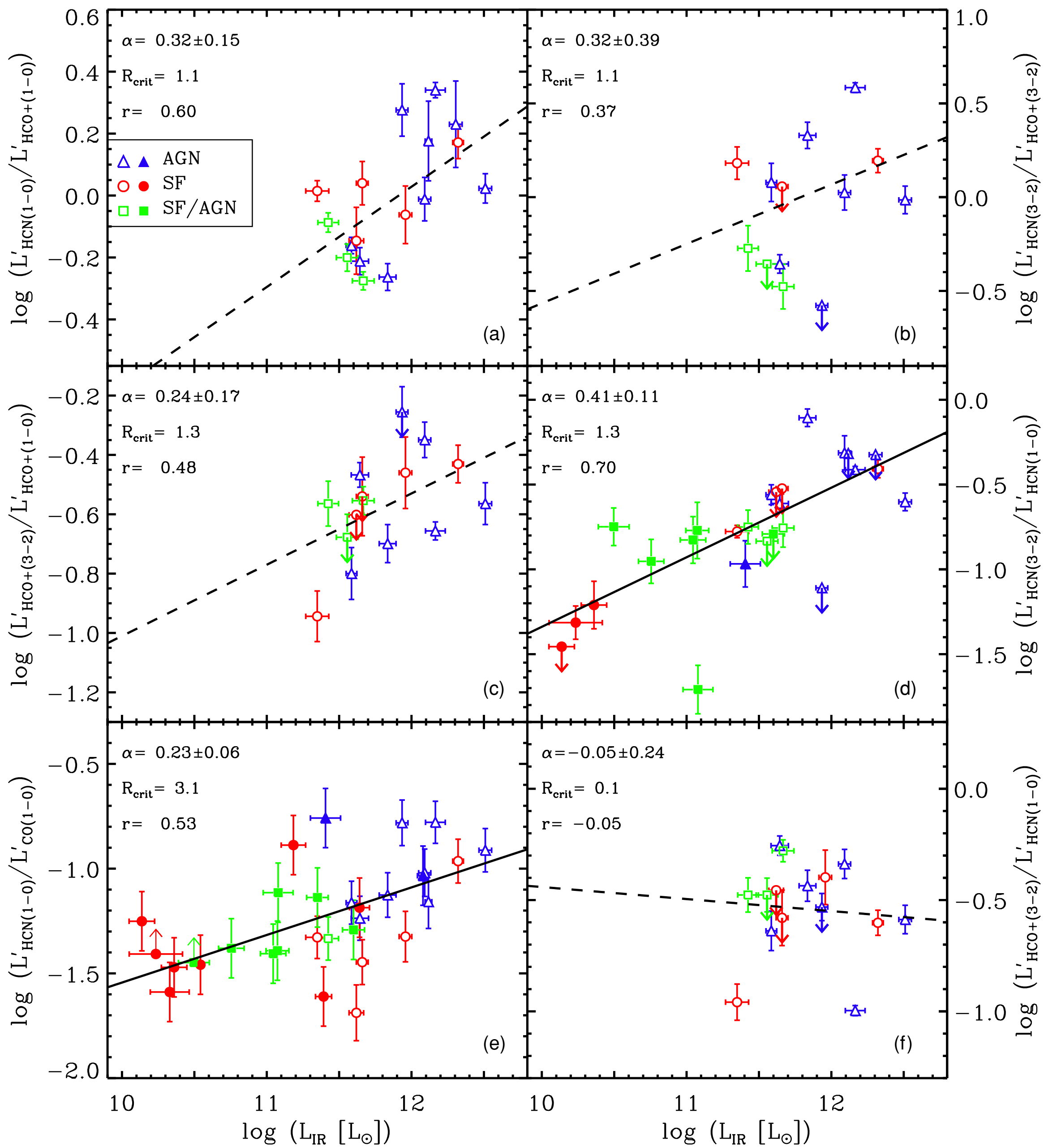

Figure 6. Molecular line luminosity ratios as a function of infrared luminosity. We compare high- and low-critical density molecular lines, $\log(L'_{\rm HD}/L'_{\rm LD})$, and label each panel with the best-fit slope (α), the ratio of the critical densities ($R_{\rm crit} \equiv \log(n_{\rm crit}^{\rm HD}/n_{\rm crit}^{\rm LD})$), and the linear correlation coefficient (r). The slope is computed for our combined sample when available (solid lines) and otherwise for the GC08 sample only (dashed lines). The line ratios used are: top left: $\mathrm{HCN}_{J=1\text{–}0}/\mathrm{HCO}^+_{J=1\text{–}0}$; top right: $\mathrm{HCN}_{J=3\text{–}2}/\mathrm{HCO}^+_{J=3\text{–}2}$; middle left: $\mathrm{HCO}^+_{J=3\text{–}2}/\mathrm{HCO}^+_{J=1\text{–}0}$; middle right: $\mathrm{HCN}_{J=3\text{–}2}/\mathrm{HCN}_{J=1\text{–}0}$; bottom left: $\mathrm{HCN}_{J=1\text{–}0}/\mathrm{CO}_{J=1\text{–}0}$; bottom right: $\mathrm{HCO}^+_{J=3\text{–}2}/\mathrm{HCN}_{J=1\text{–}0}$. The different symbols represent the optical spectral type: star-forming (SF; red circles); AGN (blue triangles); and SF/AGN (green squares). Open symbols denote galaxies from the GC08 sample, whereas filled symbols are used for galaxies in our primary sample only. Ratios shown in (g)–(j) are: (g): $\mathrm{HCO}^+_{J=1\text{–}0}/\mathrm{CO}_{J=1\text{–}0}$; (h): $\mathrm{HCN}_{J=3\text{–}2}/\mathrm{HCO}^+_{J=1\text{–}0}$; (i): $\mathrm{HCO}^+_{J=3\text{–}2}/\mathrm{CO}_{J=1\text{–}0}$; (j): $\mathrm{HCN}_{J=3\text{–}2}/\mathrm{CO}_{J=1\text{–}0}$.

(A color version of this figure is available in the online journal.)

The relations are better constrained ($>3\sigma$) for transitions for which it is possible to use our combined sample as it increases the dynamic range in IR luminosity by one order of magnitude. Cases where only the GC08 observations are available are subject to more uncertainty, and would benefit from additional measurements at lower IR luminosities to confirm the trend observed here. Nevertheless, we find a compelling case for interpreting the variations in line luminosity ratios in terms of the molecular gas density distribution.

In Figure 7, we present a compilation of the values of α shown in Figure 6. We identify the points that originate from our combined sample (red stars) and those that correspond to the GC08 sample (black circles). Although we expect other variables such as molecular gas temperature and excitation to add to the scatter around each value of α, the existence of a significant positive correlation in Figure 7 suggests that the molecular gas density distribution may be the primary physical mechanism driving the observed molecular line luminosity ratios in LIRGs and ULIRGs.

This result is consistent with the analysis of Iono et al. (2009) who find that the CO(3–2) source size is more compact than the CO(1–0) size for ULIRGs, suggesting that their high FIR (IR)

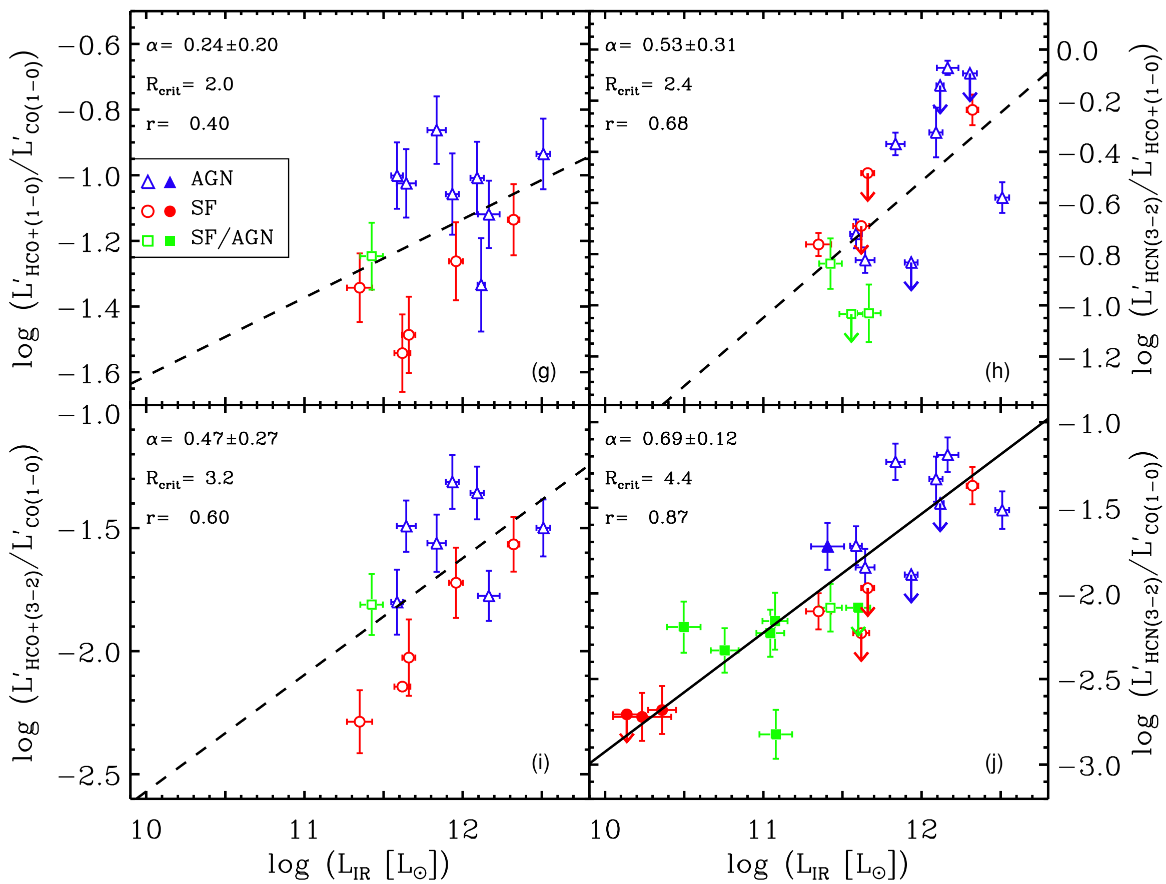

Figure 6. (Continued)

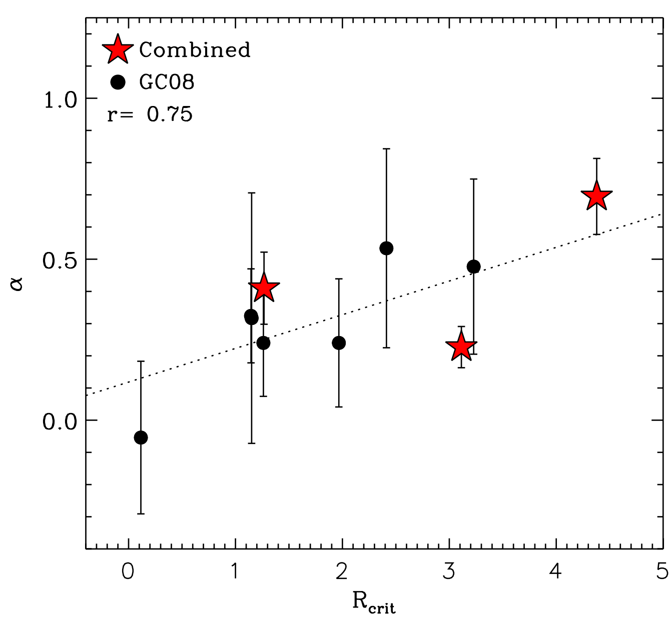

Figure 7. Values of α as a function of $R_{\rm crit}$, the logarithm of the ratio of critical densities of the lines. The index α characterizes the $L_{\rm IR}$-dependence of the molecular line luminosity ratios shown in Figure 6 (i.e., $(L'_{\rm HD}/L'_{\rm LD}) \propto (L_{\rm IR})^{\alpha}$). Most line ratios included in this figure have $R_{\rm crit} > 1$. Correspondingly, these ratios show a positive index indicating an increase toward high $L_{\rm IR}$. On the other hand, HCN(1–0) and HCO^{+}(3–2) have a similar critical density (their $R_{\rm crit}$ is close to zero), and their luminosity ratio is consistent with being constant with infrared luminosity ($\alpha = 0$). The slope distribution of the points in this figure has a mean and standard deviation of 0.10 ± 0.07 (1.5σ away from zero, dotted line).

(A color version of this figure is available in the online journal.)

luminosity is linked with them having a large amount of dense molecular gas concentrated within their central region. Furthermore, there is evidence suggesting that the ISM ambient density in ULIRGs is higher by a factor of 100 compared to normal star-forming galaxies (Solomon et al. 1997). A number of other studies support the presence of warm and dense molecular gas in these IR-bright galaxies (e.g., Lahuis et al. 2007; Armus et al. 2007).

Our findings are also in agreement with the Arp 220 and NGC 6240 case studies of Greve et al. (2009), who report an increased dense gas fraction in these two prototypical ULIRGs. Using measurements of a large number of dense molecular tracers, these authors infer that, for these two ULIRGs, most of the molecular gas is in a dense phase and that the GMCs mass-size power law is steeper than in normal star-forming galaxies, indicating that HCN emission traces denser and more compact GMCs compared to HCO+ transitions between the same J levels.

3.3. Possible Causes of Higher Gas Density

Assuming that variations in temperature and excitation are smaller than the effect of varying density, a positive relation between α and $R_{\rm crit}$ would imply that more IR-luminous galaxies have a larger fraction of dense gas than galaxies with smaller IR luminosities (see Section 4 for comparison to radiative transfer models). Several mechanisms could create such a situation (which translates to a larger average density of the molecular gas). For example, superwinds capable of expelling interstellar material have been observed in IR-bright starburst galaxies (Heckman et al. 2000). AGN-driven outflows have been modeled and are predicted to be capable of expelling molecular gas from galaxies (Narayanan et al. 2006, 2008b).

Although signatures of atomic gas outflows have been reported in a large number of studies (e.g., Heckman et al. 1990; Veilleux et al. 1995; Rupke et al. 2005; Martin 2006; Spoon & Holt 2009; for a review, see Veilleux et al. (2005)), observational evidence for large-scale outflows of molecular gas is scarce and very recent. Based on their observations of CO(3–2), HCO^+(3–2), and HCO^+(4–3), Sakamoto et al. (2009) find P Cygni profiles indicating outflows of molecular gas around the two merging nuclei of Arp 220. They also report that the HCO^+ emission is more concentrated around the nuclei relative to the CO emission, in agreement with the picture presented here, where this difference would reflect an enhanced molecular gas density in these regions. In addition, molecular gas outflows have recently been identified for the S0 galaxy NGC 1266 (K. Alatalo et al. 2010, in preparation). In this case, the outflow may be associated with the high-density enshrouded nucleus (Mouri et al. 1998), but the powering source (AGN or stellar) remains unclear. Future searches for molecular outflows in galaxies would be useful to understand their energy and gas content balance.

The gas density distribution could be affected if, for example, low-density gas is depleted more easily than denser gas during such outflows. In support of this scenario, lower density medium is expected to occupy a larger volume and would acquire larger outflow velocity by conservation of momentum. In addition, the evidence that outflow velocities increase with IR luminosity (Martin 2005; Rupke et al. 2005) is consistent, at least qualitatively, with an increase in dense gas fraction in more IR-luminous galaxies as they can more easily deplete less dense gas. On the other hand, gas accretion and inflows could counteract this effect to a certain extent and help replenish the gas content.

Alternatively, one could posit that galaxies with a larger reservoir of dense gas (and/or higher dense gas fraction) can sustain higher IR luminosity by allowing for more powerful starbursts and AGN activity. Mergers of gas-rich galaxies can trigger and fuel both starburst and AGN activity and consequently appear as ULIRGs. Indeed, most if not all of the ULIRGs in this sample are undergoing a galaxy merger. The important change in the dynamics of these systems, and in particular, of their molecular gas content might be the underlying cause of the different gas density distributions and consequently, enhanced HD/LD line luminosity ratios.

Direct comparisons between high- and low-density molecular gas tracers to interpret the physical conditions of the molecular ISM in infrared luminous galaxies were also used in Baan et al. (2008). These authors propose that the gas density distribution reflects the evolutionary stage of a nuclear outburst in (U)LIRGs. In their picture, the denser gas is depleted more rapidly than the lower density gas as the nuclear starburst progresses, and the molecular line ratios provide clues about a shift in the dominant heating source (UV versus X-ray photons).

Loenen et al. (2008) modeled some of the key molecular line ratios presented in Baan et al. (2008) and found that mechanical feedback heating is a crucial process to explain the low HNC(1–0)/HCN(1–0) ratio observed in some systems. They provide additional support for a time-dependent model of the physical conditions in the nuclear regions of luminous infrared galaxies, according to which the molecular ISM switches from a high-density ($\sim 10^5$ cm^{-3}) phase, dominated by stellar heating, to a lower density ($\sim 10^{4.5}$ cm^{-3}) phase, dominated by mechanical heating.

We explore a varying HD/LD line luminosity ratio further in the following section, where we present simulations of individual disk galaxies as well as mergers of gas-rich galaxies.

4. MODEL LINE RATIOS

In order to investigate whether X-ray-induced chemistry is necessary to drive the observed trends of line ratio with infrared luminosity (e.g., Graciá-Carpio et al. 2006), we compare observed molecular line ratios with fixed-abundance numerical simulations (Narayanan et al. 2008a).

In the left column of Figure 8, we show the model predictions, and compare them directly to the observations in the right column. The HCN and CO simulations were taken from the study of (Narayanan et al. 2008a), while HCO^+ simulations of gas-rich galaxy mergers were run specifically for this work. When available, the isolated disk galaxies include a large dynamic range of gas fractions and masses (see Section 2.1). The two galaxy merger simulations are identical in all ways except for their feedback implementation. The thick gray curve represents a galaxy merger in which 0.5% of the accreted mass energy onto the central black hole is re-injected into the surrounding ISM as thermal energy input, while the merger shown by the thin yellow curve does not include AGN feedback. Each time step of 5 h^{-1} Myr is shown with a filled triangle (circle) for the model with(without) black hole feedback. During their peak burst (when the galaxy may be most visible as a ULIRG), AGN winds can vary both the star formation history and gas density profiles in the galaxies (e.g., Springel et al. 2005). Hence, these two models effectively serve as two different galaxies probing different line ratio–$L_{\rm IR}$ relations. The infrared luminosity of the simulated galaxies is estimated from their known SFR. We use the Kennicutt (1998) conversion $L_{\rm FIR} = (5.5 \times 10^9) \times$ SFR and our observed relation $L_{\rm IR} = 1.38 \times L_{\rm FIR}$ found in Figure 2.

The molecular line luminosity ratios considered here are HCN(1–0)/CO(1–0), HCN(3–2)/CO(1–0), HCO^+(3–2)/HCO^+(1–0), and HCN(3–2)/HCN(1–0). As before, we show the galaxies overlapping with the GC08 sample with open symbols, whereas filled symbols are for observations from our primary data set only. Because galaxies with HCO^+ observations strictly belong to the GC08 sample, they occupy the brighter end of the $L_{\rm IR}$ range, which is well sampled by the merger models. The isolated gas-rich galaxies (open circles) cover the low end of the infrared luminosity, with the exception of two cases at $L_{\rm IR} \sim 10^{11.5}$–$10^{12}$ $L_\odot$, which were designed to explore extreme conditions that are physically unrealistic at low-redshift (e.g., the most massive $M_{\rm DM} \sim 10^{13}$ $M_\odot$ galaxies).

Generally speaking, there is an excellent correspondence between the range of the observations and models in their molecular line ratios. At large infrared luminosities (SFRs), the line ratios tend to increase. This effect is simply a manifestation of the fact that the galaxies at the high infrared luminosity range are undergoing a starburst event. When the fraction of dense gas in a galaxy increases (for example, owing to a merger) so does the rate at which stars form. Large amounts of dense gas also imply that starbursting galaxies are more easily able to excite high critical density tracers (such as various transitions of HCN or HCO^+), thus increasing the observed HD/LD line ratios. Because the simulations include constant, Galactic-based

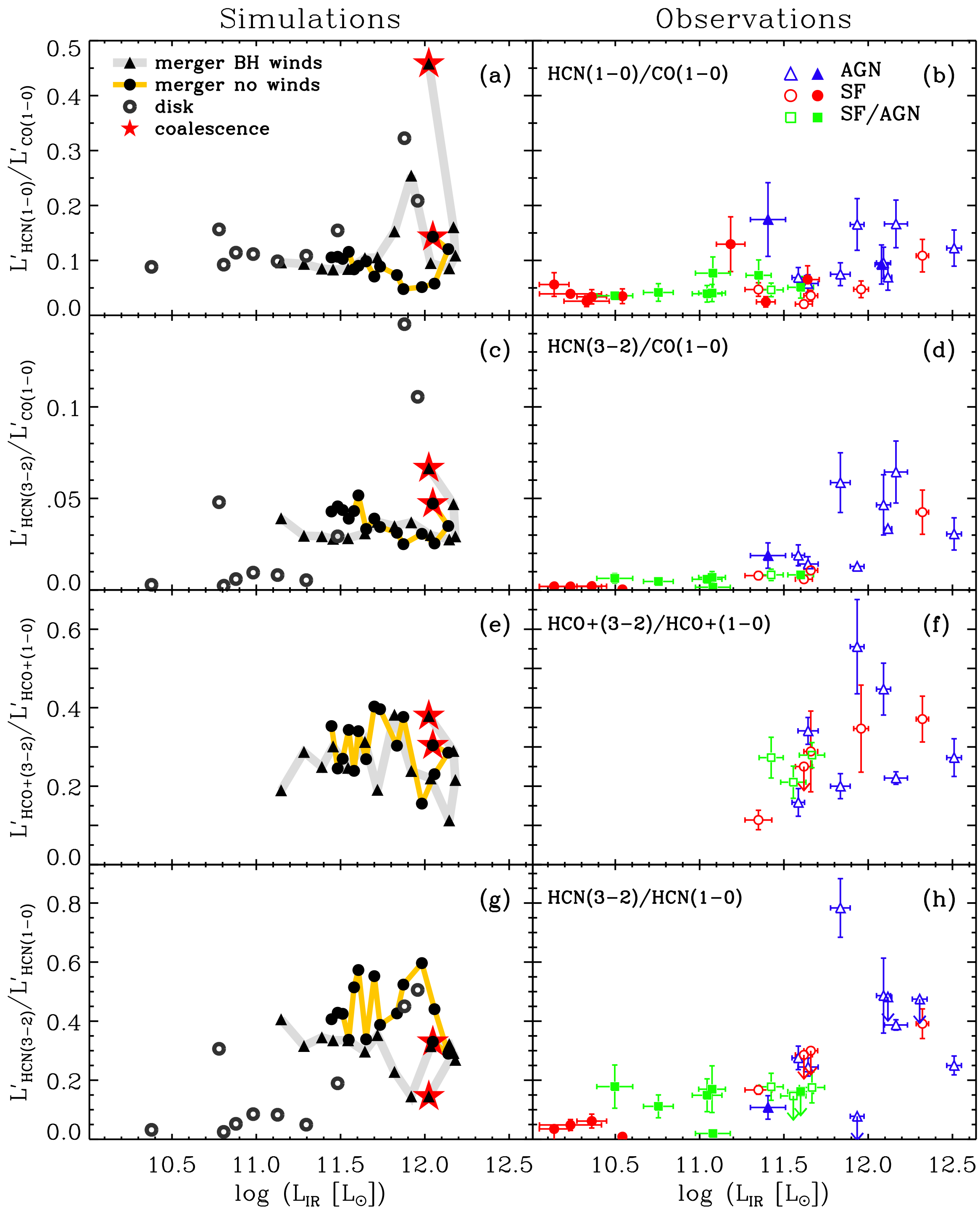

Figure 8. Several molecular line luminosity ratios as a function of infrared luminosity. The simulation results are shown in the left-hand column while the observations for the corresponding ratio are shown on the right. From top to bottom, the luminosity ratios are: HCN(1–0)/CO(1–0) (a,b), HCN(3–2)/CO(1–0) (c,d), HCO^+(3–2)/HCO^+(1–0) (e,f), and HCN(3–2)/HCN(1–0) (g,h). This figure shows evolutionary tracks of equal-mass merger simulations with (gray line) and without (yellow line) SMBH feedback combined with simulations of individual gas-rich disk galaxies (open circles). The tracks start at black-hole coalescence (large star symbol), and each time step is marked with a black symbol. Although their dynamical range differs slightly, the models successfully reproduce the spread observed in the data. Plotting symbols for the observations are as follows: star-forming galaxies (SF) (red circles); AGN (blue triangles); and SF/AGN (green squares). We use open symbols for galaxies that belong to the GC08 sample and filled symbols otherwise.

(A color version of this figure is available in the online journal.)

abundances without chemistry-driven variations, the agreement between model and data demonstrates that chemistry-driven abundance variations are not necessary to produce the observed line ratios.

We note that generally the dynamic range of the modeled line ratios seems to match the observations reasonably well. However, we urge caution with a detailed comparison of the models and the data. First, the simulations were designed to

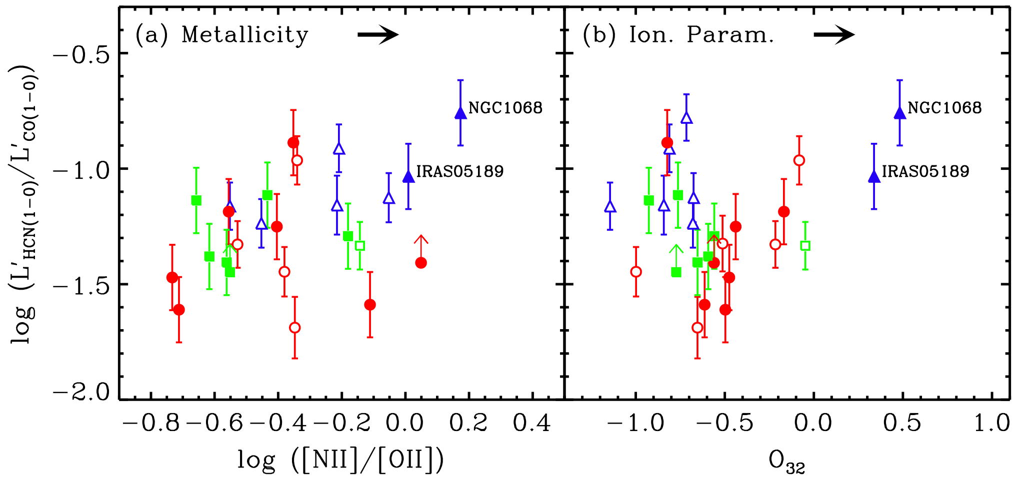

Figure 9. HCN(1–0)/CO(1–0) luminosity ratio as a function of nebular emission-line diagnostics of the diffuse ISM metallicity (left) and ionization parameter (right). There is no obvious trend except for two outliers for which the high HCN(1–0)/CO(1–0) luminosity ratio could potentially be associated with enhanced metallicity and/or ionization in the ISM. Plotting symbols represent the optical spectral type: star-forming (SF; red circles); AGN (blue triangles); and SF/AGN (green squares). We use open symbols for galaxies that belong to the GC08 sample and filled symbols otherwise.

(A color version of this figure is available in the online journal.)

probe a large parameter space in gas fractions and galaxy masses. Some galaxies were specifically designed to probe relatively extreme conditions (e.g., initial gas fractions $f_g = 0.8$, $M_{DM} \sim 10^{13}$ $M_\odot$). Consequently, individual model galaxies can be caught during a brief snapshot with extreme line ratios, and may not exactly map to a particular galaxy from observed galaxy samples in Figure 8. Second, the galaxies in the models were not chosen to precisely mimic the relative number of isolated galaxies versus mergers in the GS04a,b samples. Thus, the clustering of simulated points in Figure 8 may not exactly match those in the observations. Third, the L_{IR} in the models was calculated using a linear mapping from the SFR. While we do not consider AGN contribution to L_{IR} in the simulations, there is some in the observations. This is likely to be the reason why the observations extend to brighter L_{IR} ($>10^{12.5}$ $L_\odot$) compared to the simulations, which seem to reach a ceiling at $L_{IR} \sim 10^{12.2}$ $L_\odot$.

5. POSSIBLE CHEMISTRY EFFECTS

It has been suggested that the radiation field associated with an AGN influences the abundance of HCN with respect to other molecules. For example, emitted X-rays could cause X-ray-dominated regions (XDRs), which have different properties than regular photon-dominated regions (PDRs) found around star-forming regions. Previous authors claim that conditions existing in these XDRs affect molecular gas abundance (Lintott & Viti 2006; Aalto et al. 2007; Krips 2007).

On the other hand, Baan et al. (2008) used multiple molecular line ratios to distinguish between XDR and PDR conditions, and found that most of the (U)LIRGs in their sample are dominated by PDRs. They used tracers sensitive to column density (N_H) to distinguish between an elevated HCN/CO intensity ratio resulting from a high-N_H PDR or from a low-N_H XDR, and found the former to be more likely.

In this section, we present optical spectral diagnostics associated with ISM metallicity and ionization parameter (Figure 9). The emission-line ratio [N II] λ6584/[O II] λ3727 has been shown to correlate with the gas-phase oxygen abundance 12 + log(O/H) while being less affected by the presence of an AGN than other metallicity diagnostics (Kewley & Dopita 2002; Kewley & Ellison 2008). Meanwhile, the emission-line ratio $O_{32} \equiv \log([\mathrm{O\,III}]\,\lambda5007/[\mathrm{O\,II}]\,\lambda3727)$ traces the ionization parameter. The correspondence between the observed ratio and the ionization depends slightly on the metallicity so the two panels of Figure 9 should be interpreted in conjunction.

Most galaxies are scattered without obvious trends in the HCN(1–0)/CO(1–0)–[N II] λ6584/[O II] λ3727 and HCN(1–0)/CO(1–0)–O_{32} planes. The correlations are very weak or non-existent, especially if we exclude the two outliers (IRAS 05189−2524 and the more extreme NGC 1068). In the first panel, the correlation coefficient $r = 0.42$ drops to $r = 0.24$ if we exclude NGC 1068 and down further to $r = 0.15$ if we exclude both outliers mentioned above. In the second panel, the correlation coefficient drops from $r = 0.26$ to $r = -0.09$ if we exclude both outliers. NGC 1068 (and possibly IRAS 05189−2524) may be a special case where unusual ionization or chemistry effects could play a significant role in producing the observed HCN(1–0)/CO(1–0) luminosity ratios.

Our result is in agreement with findings of Usero et al. (2004) who conclude that the circumnuclear region of NGC 1068 is effectively a giant XDR. These authors used a combination of single dish and interferometry data of several molecular species to rule out alternative explanations for the observed high HCN/CO ratio (Tacconi et al. 1994). NGC 1068 is also observed to have the largest MIR-excess (it lies 4.5σ from the mean on Figure 2), a regime where MIR-pumping can promote HCN(1–0) emission by exciting a bending mode at 14 μm (Aalto et al. 1995).

While the optical emission-line ratios used here may give a good indication of the metallicity and ionization state of the diffuse ISM, it is not clear how representative they are of the conditions present in denser molecular gas. Therefore, it may not be surprising that we do not see obvious trends in either panel. This caveat is especially important if young stars (starburst) are the main source of ionization because UV photons do not penetrate deeply into the dense molecular. On the other hand, X-ray photons can penetrate through much larger column densities of material, so it is plausible that the extreme conditions triggered by an AGN would occur over a large enough volume to effect both the diffuse and dense gas phases. If this were the case, we would expect a larger HCN(1–0)/CO(1–0) luminosity ratio to couple with larger values of O_{32} because an increased ionization means more free electrons, which can accelerate the production of HCN molecules (as discussed in Section 1).

Overall, our results indicate that cases with a genuine abundance change in HCN may exist but are the exception rather than the rule.

6. CONCLUSIONS

Using a sample of 34 nearby infrared luminous galaxies ($10^{10}\ L_\odot < L_{\rm IR} < 10^{12.5}\ L_\odot$), we characterized the infrared luminosity dependence of various molecular gas tracers.

1. The presence of the AGNs was assessed using the optical BPT diagram. In agreement with previous publications, we find a more frequent occurrence of AGN in more IR-luminous galaxies. This may be related to the availability of larger amounts of dense gas during the mergers of gas-rich galaxies.
2. The molecular transitions used, CO(1–0), HCO^+(1–0), HCN(1–0), HCO^+(3–2), and HCN(3–2), span four orders of magnitude in critical density. We find that the relationship between (F)IR luminosity and molecular line luminosity $L_{\rm mol}$ is shallower for transitions with higher $n_{\rm crit}$. This trend is in agreement with theoretical models of Narayanan et al. (2008a) and Krumholz & Thompson (2007) and can be explained by the varying degree of thermalization of the gas giving rise to molecular line emission.
3. Trends of molecular line ratios with $L_{\rm IR}$ are consistent with an increased molecular gas density in more IR-bright galaxies. This result agrees with the picture presented by Gao & Solomon (2004b) and Wu et al. (2005). When comparing high-density and low-density molecular gas tracers, we observe an increase in their luminosity ratio ($L_{\rm HD}/L_{\rm LD}$) with increasing infrared luminosity. Interestingly, this trend vanishes when comparing two tracers with nearly equal critical density (HCN(1–0) and HCO^+(3–2)). We infer that the main driver of the enhanced HD/LD luminosity ratio is the molecular gas density distribution, in agreement with the observations that ULIRGs host large reservoirs of dense molecular gas in their central regions.
4. We compare our observed molecular line ratios with theoretical values obtained from a set of galaxy models. We consider SPH simulations of two galaxy mergers as well as individual gas-rich galaxies. With constant Galactic abundances, the models successfully produce enhanced HD/LD luminosity ratios at brighter infrared luminosity. This provides additional support for a higher molecular gas density in galaxies that are extremely gas-rich or undergoing gas-rich mergers. Indeed, this result suggests that AGN-induced chemistry (or other) effects may not be necessary to reproduce the observations, but rather that AGNs are more likely to reside in galaxies that are very gas-rich and/or experiencing a merger. The simulations also demonstrate important variations in molecular luminosity ratio with the evolutionary stage of the mergers. These variations may be connected with the dynamics of the molecular gas during mergers (inflows, outflows, gas compression, etc.).
5. We investigate possible chemistry effects on the well-known HCN(1–0)/CO(1–0) luminosity ratio using common optical emission-line diagnostics of the ISM ionization parameter and metallicity. With the exception of one of two outliers, we do not observe significant correlations between the molecular line ratio and these properties. Decoupling between the dense molecular gas traced by CO(1–0) and HCN(1–0) and the more diffuse gas that traces the optical nebular line may be responsible for the absence of correlation. However, we note that NGC 1068 shows extreme conditions in the sense of having the largest optically measured ionization parameter as well as the largest MIR-excess. This outlier is thus more subject to chemistry and/or MIR-pumping effects quoted in the literature. We emphasize that NGC 1068 has properties that are very distinct from the rest of our sample, and thus may not be representative of its class.
6. More high-density molecular line observations would be extremely beneficial to confirm the trends outlined in this work. Only half of our combined sample of 34 galaxies have data for all five molecular lines used here. In particular, future observations should target galaxies with fainter IR luminosities to test whether the results presented here extend into the lower luminosity regime. Higher resolution studies of high-density tracers may complement this work by allowing for a more detailed analysis of the density and excitation structure of the molecular gas within galaxies. Such studies could provide information on the *local* influence of an AGN, whereas in this work we probe the *global* influence of an AGN.
7. Overall, our results support that HCN(1–0) is a valid tracer of dense molecular gas in galaxies even in the presence of an AGN. We expect scatter in the relationship due to variations in temperature and possible radiative (de-)excitation of this transition. Also, the dense-to-total molecular gas fraction is expected to differ from galaxy to galaxy, especially in systems undergoing significant mergers.

The authors thank Yu Gao and Neal Evans for useful comments and Leo Blitz for sharing early results about molecular outflows. This work also benefited from invaluable input from Willem Baan & Javier Gracía-Carpio. We are grateful to the anonymous referee for a constructive report which helped improve this manuscript. S.J. acknowledges Mark Dickinson for his support and advice. S.J. was partially funded by an FQRNT doctoral fellowship (Québec, Canada).

This research has made use of the NASA/IPAC Extragalactic Database (NED), which is operated by the Jet Propulsion Laboratory, California Institute of Technology, under contract with the National Aeronautics and Space Administration.

APPENDIX

OBSERVED HCN(3–2) SPECTRA

The Heinrich Hertz Submillimeter Telescope (HHT) HCN(3–2) spectra from the survey presented in Bussmann et al. (2008) are displayed in Figure 10.

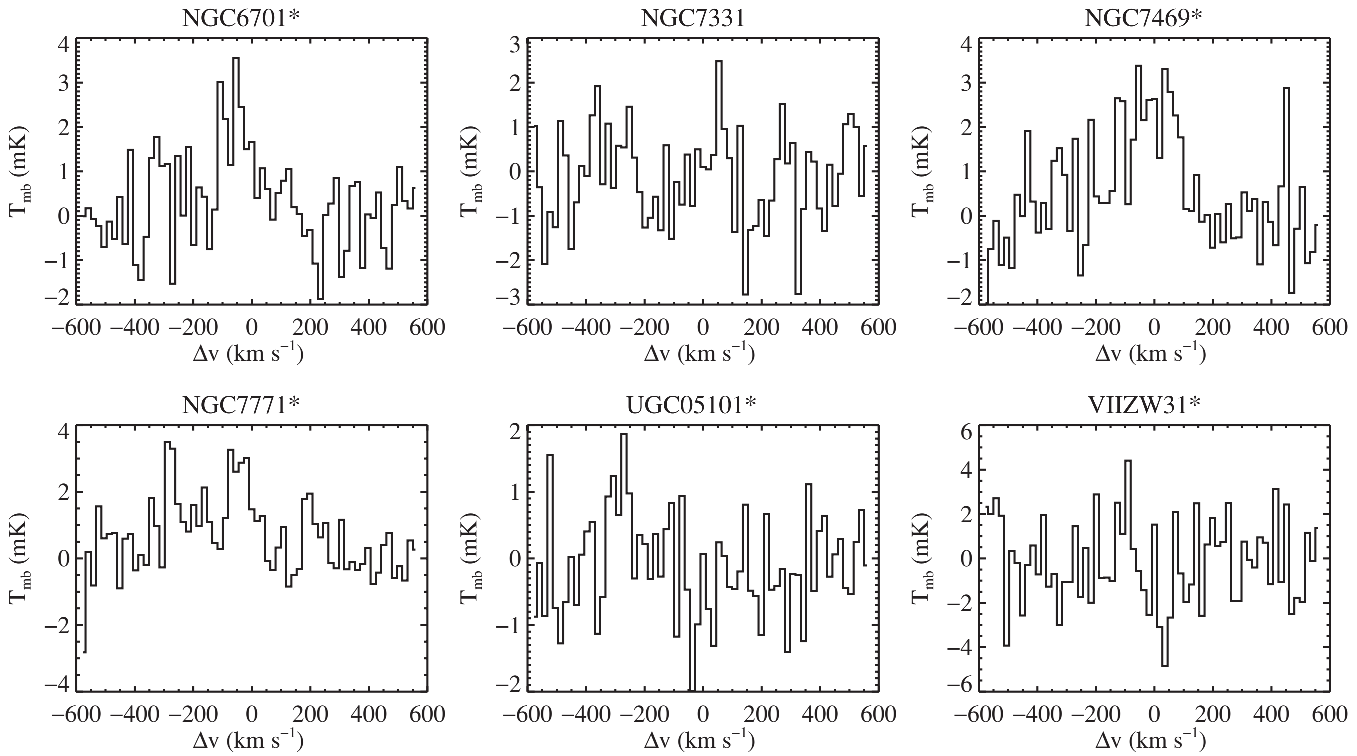

Figure 10. HCN(3–2) spectra for all galaxies observed in B08. The 23 galaxies overlapping with this sample are marked with an asterisk. One galaxy was mapped (NGC 253, plus symbol). These observations were combined with the HCN(3–2) data presented in GC08 as described in Section 2.1.

(An extended version of this figure is available in the online journal.)

REFERENCES

Aalto, S., Booth, R. S., Black, J. H., & Johansson, L. E. B. 1995, A&A, 300, 369
Aalto, S., Spaans, M., Wiedner, M. C., & Hüttemeister, S. 2007, A&A, 464, 193
Abazajian, K. N., et al. 2009, ApJS, 182, 543
Armus, L., et al. 2007, ApJ, 656, 148
Baan, W. A., Henkel, C., Loenen, A. F., Baudry, A., & Wiklind, T. 2008, A&A, 477, 747
Baldwin, J. A., Phillips, M. M., & Terlevich, R. 1981, PASP, 93, 5
Bell, E. F. 2003, ApJ, 586, 794
Blitz, L., & Rosolowsky, E. 2006, ApJ, 650, 933
Brinchmann, J., Charlot, S., White, S. D. M., Tremonti, C., Kauffmann, G., Heckman, T., & Brinkmann, J. 2004, MNRAS, 351, 1151
Bussmann, R. S., et al. 2008, ApJ, 681, L73 (B08)
Condon, J. J., Huang, Z.-P., Yin, Q. F., & Thuan, T. X. 1991, ApJ, 378, 65
Elvis, M., et al. 1994, ApJS, 95, 1
Evans, N. J., II. 1999, ARA&A, 37, 311
Farrah, D., Afonso, J., Efstathiou, A., Rowan-Robinson, M., Fox, M., & Clements, D. 2003, MNRAS, 343, 585
Farrah, D., et al. 2007, ApJ, 667, 149
Gao, Y., & Solomon, P. M. 2004a, ApJS, 152, 63 (GS04a)
Gao, Y., & Solomon, P. M. 2004b, ApJ, 606, 271 (GS04b)
Genzel, R., et al. 1998, ApJ, 498, 579
Gordon, K. D., Clayton, G. C., Witt, A. N., & Misselt, K. A. 2000, ApJ, 533, 236
Graciá-Carpio, J., García-Burillo, S., Planesas, P., & Colina, L. 2006, ApJ, 640, L135
Graciá-Carpio, J., García-Burillo, S., Planesas, P., Fuente, A., & Usero, A. 2008, A&A, 479, 703 (GC08)
Greve, T. R., Papadopoulos, P. P., Gao, Y., & Radford, S. J. E. 2009, ApJ, 692, 1432
Heckman, T. M., Armus, L., & Miley, G. K. 1990, ApJS, 74, 833
Heckman, T. M., Lehnert, M. D., Strickland, D. K., & Armus, L. 2000, ApJS, 129, 493
Imanishi, M. 2009, ApJ, 694, 751
Iono, D., et al. 2009, ApJ, 695, 1537
Kauffmann, G., et al. 2003, MNRAS, 346, 1055
Kelly, B. C. 2007, ApJ, 665, 1489
Kennicutt, R. C., Jr. 1989, ApJ, 344, 685
Kennicutt, R. C., Jr. 1998, ApJ, 498, 541
Kewley, L. J., & Dopita, M. A. 2002, ApJS, 142, 35
Kewley, L. J., & Ellison, S. L. 2008, ApJ, 681, 1183
Kewley, L. J., Heisler, C. A., Dopita, M. A., & Lumsden, S. 2001, ApJS, 132, 37
Krips, M., Neri, R., García-Burillo, S., Martín, S., Combes, F., Graciá-Carpio, J., & Eckart, A. 2008, ApJ, 677, 262
Krips, M., et al. 2007, A&A, 468, L63
Krumholz, M. R., & Thompson, T. A. 2007, ApJ, 669, 289
Lahuis, F., et al. 2007, ApJ, 659, 296
Le Floc'h, E., Mirabel, I. F., Laurent, O., Charmandaris, V., Gallais, P., Sauvage, M., Vigroux, L., & Cesarsky, C. 2001, A&A, 367, 487
Levine, E. S., Helfer, T. T., Meijerink, R., & Blitz, L. 2008, ApJ, 673, 183
Lintott, C., & Viti, S. 2006, ApJ, 646, L37
Loenen, A. F., Spaans, M., Baan, W. A., & Meijerink, R. 2008, A&A, 488, L5
Lutz, D., et al. 1996, A&A, 315, L137
Lutz, D., Spoon, H. W. W., Rigopoulou, D., Moorwood, A. F. M., & Genzel, R. 1998, ApJ, 505, L103
Martin, C. L. 2005, ApJ, 621, 227
Martin, C. L. 2006, ApJ, 647, 222
Mo, H. J., Mao, S., & White, S. D. M. 1998, MNRAS, 295, 319
Mouri, H., Taniguchi, Y., Sato, Y., & Kawara, K. 1998, A&A, 334, 482
Moustakas, J., & Kennicutt, R. C., Jr. 2006, ApJS, 164, 81 (MK06)
Moustakas, J., Kennicutt, R. C., Jr., & Tremonti, C. A. 2006, ApJ, 642, 775
Narayanan, D., Cox, T. J., Shirley, Y., Davé, R., Hernquist, L., & Walker, C. K. 2008a, ApJ, 684, 996
Narayanan, D., Groppi, C. E., Kulesa, C. A., & Walker, C. K. 2005, ApJ, 630, 269
Narayanan, D., et al. 2006, ApJ, 642, L107
Narayanan, D., et al. 2008b, ApJS, 176, 331
Nardini, E., Risaliti, G., Salvati, M., Sani, E., Imanishi, M., Marconi, A., & Maiolino, R. 2008, MNRAS, 385, L130
Osterbrock, D. E. 1989, Astrophysics of Gaseous Nebulae and Active Galactic Nuclei (Mill Valley, CA: Univ. Science Books)
Rieke, G. H., Cutri, R. M., Black, J. H., Kailey, W. F., McAlary, C. W., Lebofsky, M. J., & Elston, R. 1985, ApJ, 290, 116

Rupke, D. S., Veilleux, S., & Sanders, D. B. 2005, ApJS, 160, 115
Sakamoto, K., et al. 2009, ApJ, 700, L104
Sanders, D. B., Mazzarella, J. M., Kim, D.-C., Surace, J. A., & Soifer, B. T. 2003, AJ, 126, 1607
Sanders, D. B., & Mirabel, I. F. 1996, ARA&A, 34, 749
Schmidt, M. 1959, ApJ, 129, 243
Schöier, F. L., van der Tak, F. F. S., van Dishoeck, E. F., & Black, J. H. 2005, A&A, 432, 369
Solomon, P. M., Downes, D., & Radford, S. J. E. 1992, ApJ, 387, L55
Solomon, P. M., Downes, D., Radford, S. J. E., & Barrett, J. W. 1997, ApJ, 478, 144
Spoon, H. W. W., & Holt, J. 2009, ApJ, 702, L42
Spoon, H. W. W., Marshall, J. A., Houck, J. R., Elitzur, M., Hao, L., Armus, L., Brandl, B. R., & Charmandaris, V. 2007, ApJ, 654, L49
Springel, V. 2005, MNRAS, 364, 1105
Springel, V., Di Matteo, T., & Hernquist, L. 2005, MNRAS, 361, 776
Springel, V., & Hernquist, L. 2003, MNRAS, 339, 289
Tacconi, L. J., Genzel, R., Blietz, M., Cameron, M., Harris, A. I., & Madden, S. 1994, ApJ, 426, L77
Tremonti, C. A., et al. 2004, ApJ, 613, 898
Usero, A., García-Burillo, S., Fuente, A., Martín-Pintado, J., & Rodríguez-Fernández, N. J. 2004, A&A, 419, 897
Vega, O., Clemens, M. S., Bressan, A., Granato, G. L., Silva, L., & Panuzzo, P. 2008, A&A, 484, 631
Veilleux, S., Cecil, G., & Bland-Hawthorn, J. 2005, ARA&A, 43, 769
Veilleux, S., Kim, D.-C., & Sanders, D. B. 1999, ApJ, 522, 113
Veilleux, S., Kim, D.-C., Sanders, D. B., Mazzarella, J. M., & Soifer, B. T. 1995, ApJS, 98, 171
Veilleux, S., & Osterbrock, D. E. 1987, ApJS, 63, 295
Veilleux, S., et al. 2009, ApJS, 182, 628
Wu, H., Zou, Z. L., Xia, X. Y., & Deng, Z. G. 1998, A&AS, 132, 181
Wu, J., Evans, N. J., II, Gao, Y., Solomon, P. M., Shirley, Y. L., & Vanden Bout, P. A. 2005, ApJ, 635, L173
York, D. G., et al. 2000, AJ, 120, 1579